

Long-term dynamical evolution of pallene (Saturn XXXIII) and its diffuse, dusty ring

Marco A. Muñoz-Gutiérrez, A. P. Granados Contreras, Gustavo Madeira, Joseph A. A'Hearn, Silvia Giuliatti Winter

▶ **To cite this version:**

Marco A. Muñoz-Gutiérrez, A. P. Granados Contreras, Gustavo Madeira, Joseph A. A'Hearn, Silvia Giuliatti Winter. Long-term dynamical evolution of pallene (Saturn XXXIII) and its diffuse, dusty ring. Monthly Notices of the Royal Astronomical Society, 2021, 10.1093/mnras/stab3627 . insu-03589767

HAL Id: insu-03589767

https://insu.hal.science/insu-03589767

Submitted on 20 Apr 2023

HAL is a multi-disciplinary open access archive for the deposit and dissemination of scientific research documents, whether they are published or not. The documents may come from teaching and research institutions in France or abroad, or from public or private research centers.

L'archive ouverte pluridisciplinaire **HAL**, est destinée au dépôt et à la diffusion de documents scientifiques de niveau recherche, publiés ou non, émanant des établissements d'enseignement et de recherche français ou étrangers, des laboratoires publics ou privés.

Monthly Notices of the ROYAL ASTRONOMICAL SOCIETY

MNRAS **511,** 4202–4222 (2022) https://doi.org/10.1093/mnras/stab3627
Advance Access publication 2021 December 15

Long-term dynamical evolution of Pallene (Saturn XXXIII) and its diffuse, dusty ring

Marco A. Muñoz-Gutiérrez [1]★ A. P. Granados Contreras [1] Gustavo Madeira [2,3] Joseph A. A'Hearn[4] and Silvia Giuliatti Winter[2]

[1]*Institute of Astronomy and Astrophysics, Academia Sinica, 11F of AS/NTU Astronomy-Mathematics Building, No.1, Section 4, Roosevelt Rd, Taipei 10617, Taiwan, R.O.C.*
[2]*Grupo de Dinâmica Orbital e Planetologia, São Paulo State University (UNESP), 333 Av. Dr. Ariberto Pereira da Cunha, Guaratinguetá, SP 12516-410, Brazil*
[3]*Université de Paris, Institut de Physique du Globe de Paris, CNRS, F-75005 Paris, France*
[4]*Department of Physics, University of Idaho, 875 Perimeter Drive, Moscow, ID 83844, USA*

Accepted 2021 December 10. Received 2021 December 10; in original form 2020 December 1

ABSTRACT

The distinctive set of Saturnian small satellites, Aegaeon, Methone, Anthe, and Pallene, constitutes an excellent laboratory to understand the evolution of systems immersed in co-orbital dusty rings/arcs, subjected to perturbations from larger satellites and non-gravitational forces. In this work, we carried out a comprehensive numerical exploration of the long-term evolution of Pallene and its ring. Through frequency map analysis, we characterized the current dynamical state around Pallene. A simple tidal evolution model serves to set a time frame for the current orbital configuration of the system. With detailed short- and long-term *N*-body simulations we determine whether Pallene is currently in resonance with one or more of six of Saturn's major moons. We analysed a myriad of resonant arguments extracted from the direct and indirect parts of the disturbing function, finding that Pallene is not in mean motion resonance from the present up to 5 Myr into the future; none the less, some resonant arguments exhibit intervals of libration and circulation at different time-scales and moon pairings. We studied the dynamical evolution of micrometric particles forming the ring, considering gravitational and non-gravitational forces. Non-gravitational forces are responsible for particles vertical excursions and outward migration. By estimating the satellite's mass production rate, we find that Pallene could be responsible for keeping its ring in steady-state only if it is mainly composed of large micrometre-sized particles. If mainly composed of particles with a few micrometres for which Pallene is the only source, the ring will spread out, both radially and vertically, until it finally disappears.

Key words: methods: numerical – planets and satellites: dynamical evolution and stability – planets and satellites: individual: Pallene – planets and satellites: rings.

1 INTRODUCTION

Pallene (Saturn XXXIII) is a satellite of only 2.23 km in radius (Thomas et al. 2013), orbiting Saturn at an average distance of ∼ 212 283 km, with an eccentricity of ∼0.004, and a relatively large inclination of ∼0.18° (Spitale et al. 2006; Jacobson et al. 2008).

This small Saturnian moon was first observed in a single photograph of the *Voyager 2* spacecraft. It was reported, together with a preliminary orbital and physical characterization, by Synnott (1986). Pallene was then rediscovered in 2005 by the *Cassini* Imaging Science team (Porco et al. 2005) and positively identified as the S/1981 S14 object from *Voyager 2*.

Pallene is one of three small moons located between the orbits of Mimas and Enceladus, called collectively as the Alkyonides. Despite the presence of a vast number of resonances in the region, accentuated by the commensurabilities of Mimas with Tethys and Enceladus with Dione (see e.g. Sinclair 1972; Greenberg 1973; Peale 1976, 1999), Pallene does not seem to be in a mean motion resonance (MMR), unlike Methone and Anthe, trapped in 14:15 and 10:11 corotation eccentricity resonances with Mimas, respectively (Cooper et al. 2008; Hedman et al. 2009; El Moutamid, Sicardy & Renner 2014). None the less, Pallene is migrating away from Saturn via tidal evolution, though at a slower rate than Mimas. Thus, the orbits of Pallene and Mimas are converging, which at some point either in the past or in the future should have resulted or should result in Pallene being captured into resonance with Mimas. A simple tidal evolution model (Murray & Dermott 1999) suggests that the most recent first-order resonance that Pallene might have escaped from, perhaps around 40 Myr ago, is the 4:5 resonance with Mimas. Pallene's current eccentricity or inclination could be signs of this or another past resonance.

After Pallene's rediscovery, Spitale et al. (2006) determined the orbital parameters of Pallene with high accuracy using images from *Cassini* and *Voyager 2*. Spitale et al. suggested that Pallene could be in an inner third-order resonance with Enceladus (i.e. $\phi = 19\lambda_{\rm Enc} - 16\lambda_{\rm Pal} - \varpi_{\rm Pal} - 2\Omega_{\rm Pal}$). However, recent short-term numerical

★ E-mail: mmunoz@asiaa.sinica.edu.tw

© 2021 The Author(s)
Published by Oxford University Press on behalf of Royal Astronomical Society

Downloaded from https://academic.oup.com/mnras/article/511/3/4202/6462913 by INIST-CNRS INSU user on 20 April 2023

integrations have shown that this resonance's libration angle actually circulates (e.g. fig. 1 in Muñoz-Gutiérrez & Giuliatti Winter 2017).

Furthermore, synchronous periodic eccentricity and inclination oscillations were found while exploring a longer term dynamical evolution of Pallene (of up to 10^5 yr, Callegari & Yokoyama 2010; Muñoz-Gutiérrez & Giuliatti Winter 2017), which could be the result of a resonant perturbation produced by either Mimas or Enceladus. Moreover, Callegari & Yokoyama (2010) identify a possible argument for the proposed quasi-resonance involving the apsidal and nodal longitudes of Pallene and Mimas, given by $\phi = \varpi_{\rm Pal} - \varpi_{\rm Mim} + \Omega_{\rm Pal} - \Omega_{\rm Mim}$. None the less, Muñoz-Gutiérrez & Giuliatti Winter (2017) found that this argument also circulates with a period of ∼4762.2 yr, though, interestingly, with the same period of the observed oscillations of Pallene's eccentricity and inclination.

Pallene shares its orbit with a diffuse ring of micrometre-sized dust, first reported by Hedman et al. (2009). The constant resupply of ring material is expected to come from impact debris, expelled from the satellite's surface by collisions between interplanetary dust particles (IDPs) and the moon. A similar mechanism has been proposed and explored in order to explain the existence of Aegaeon's ring arc inside the G ring (Hedman et al. 2010; Madeira et al. 2018), the ring arcs of Methone and Anthe (Sun et al. 2017; Madeira & Giuliatti Winter 2020), and the Neptunian rings and arcs (Gaslac Gallardo et al. 2020; Giuliatti Winter, Madeira & Sfair 2020).

In this work, we carry out a comprehensive study of the long-term dynamics of Pallene, as well as of the possible origin and dynamical evolution of its diffuse dusty ring, formed by micrometre-sized particles subject to gravitational and non-gravitational forces. We organize this paper as follows: in Section 2, we describe the different set-ups of our numerical simulations, performed to address various aspects of our study; we characterize the current dynamical environment of Pallene and its ring through frequency map analysis in Section 3. In Section 4, we first estimate the time span in which the current orbital configuration of the Saturnian system would remain approximately unchanged using a simple tidal evolution model; then, with detailed short- and long-term simulations, we re-evaluate at different time-scales all possible libration angles between Pallene and the six major Saturnian satellites considered in our study. Finally, a characterization of the evolution of Pallene's ring is carried out in Section 5, where all the relevant non-gravitational forces that affect small particles are considered. We summarize our work and present our main conclusions in Section 6.

2 METHODS AND SIMULATIONS

We carried out extensive and detailed numerical simulations of the evolution of the dynamical system formed by Pallene and six major Saturnian satellites, those gravitationally relevant in our region of interest, namely: Mimas, Enceladus, Tethys, Dione, Rhea, and Titan. Throughout this work, we consider Saturn's oblateness and take into account zonal harmonic terms up to J_6 in all simulations. Our numerical integrations cover several time spans, in order to study different aspects of the dynamics of Pallene, its phase-space surroundings, as well as the evolution of its dust-ring. Our shortest simulation lasts 18 yr, while the longest simulation is 5×10^6 yr long.

Unless otherwise stated, the physical parameters of Saturn and the six major moons used throughout this work are summarized in Tables 1 and 2. We use a rotation rate for Saturn $\Omega_{\rm S} = 1.65269 \times 10^{-4}$ rad s^{-1} from Helled et al. (2015). As initial conditions for the major Saturnian moons, we use the satellite's Saturn-centric state vectors taken from the JPL Horizons ephemerides service[1] on $JD = 2459305.5$, corresponding to 2021 April 1. We scale the satellite semimajor axes and masses to Pallene's semimajor axis and Saturn's mass, respectively. The system's gravitational constant is scaled accordingly, for which we use Pallene's average semimajor axis $\bar{a}_{\rm Pal} = 2.1228335 \times 10^5$ km (as found in Muñoz-Gutiérrez & Giuliatti Winter 2017) and the $GM_{\rm S}$ parameter given in Table 1. Consequently, our gravitational constant for this system is $G = 29.59895344398\ \bar{a}_{\rm Pal}^3\ M_{\rm S}^{-1}\ d^{-2}$.

Pallene's mass is derived from its size, which has been measured with small uncertainty, i.e. $R_{\rm Pal} = 2.23 \pm 0.07$ km, as well as from its reported range of bulk density, i.e. 0.19 g cm^{-3} $\leq \rho_{\rm Pal} \leq$ 0.34 g cm^{-3} (Thomas et al. 2013). We explore three different density values to cover the uncertainty reported by Thomas et al., i.e. $\rho_{\rm Pal} = 0.19$, 0.25, and 0.34 g cm^{-3}. This means that for each simulation suite described in the following paragraphs, we run three versions, each with Pallene's gravitational parameter given by $GM_{\rm Pal} = 5.89064055531$E-07, 7.75084283594E-07, and 1.05411462568E-06 km^3 s^{-2}, corresponding to the selected density values. At the end of each of our integrations, we convert the state vectors ($\vec{r}$ and $\vec{v}$) to geometric orbital elements (Renner & Sicardy 2006), which reduces the short-term oscillations of the osculating elements due to the oblateness of the central mass.

In order to place Pallene within its current dynamical context, our first objective is to characterize the dynamics of a broad region of the geometric semimajor axis-eccentricity (a–e) phase-space plane around Pallene. With this in mind, we performed two numerical simulations (lasting 18 and 10^4 yr, respectively), including a total of 13 025 test particles covering a grid of the geometric a–e plane in

Table 1. Saturn's physical parameters.

Parameter	Value	Reference
$R_{\rm S}$ [km]	60 330	Kliore et al. (1980)
$GM_{\rm S}$ [km^3 s^{-2}]	3.793120749865220E + 07	*gm_de431.tpc*[a]
J_2	1.6290573E-02	Iess et al. (2019)
J_4	−9.35314E-04	Iess et al. (2019)
J_6	8.6340E-05	Iess et al. (2019)
$\Omega_{\rm S}$ [rad s^{-1}]	1.65269E-04	Helled, Galanti & Kaspi (2015)

Note.[a] Available at https://naif.jpl.nasa.gov/pub/naif/generic_kernels/pck/gm_de431.tpc

Table 2. Summary of physical parameters of the six large moons in our system.

Name	GM_m [a] [km^3 s^{-2}]	ρ_m [g cm^{-3}]	R_m [b] [km]
Mimas	2.503522884661795E + 00	1.152	198.2
Enceladus	7.211292085479989E + 00	1.606	252.6
Tethys	4.121117207701302E + 01	0.956	537.5
Dione	7.311635322923193E + 01	1.469	561.4
Rhea	1.539422045545342E + 02	1.233	763.8
Titan	8.978138845307376E + 03	1.880	2574.7

Notes.[a] GM_m values are taken from the planetary constant kernel *gm_de431.tpc*.
[b] Radius values, R_m, are taken from the planetary constant kernel *pck00010.tpc* (available at https://naif.jpl.nasa.gov/pub/naif/generic_kernels/pck/pck00010.tpc, Archinal et al. 2011).

[1] https://ssd.jpl.nasa.gov/horizons.cgi

Downloaded from https://academic.oup.com/mnras/article/511/3/4202/6462913 by INIST-CNRS INSU user on 20 April 2023

the vicinity of Pallene. For these integrations, we used the Bulirsch–Stoer integrator from the MERCURY6 package (Chambers 1999), with a toleration accuracy parameter of 10^{-12} and an initial time-step of 0.1 d.

Secondly, to examine the big picture of Pallene's tidal evolution, we use a simple model based on Murray & Dermott (1999), which assumes a linear tidal dissipation mechanism and a constant Q, independent of frequency. We only examine the tidal evolution of Pallene and the large moons in its vicinity, Mimas and Enceladus, in order to look at resonances that may have been crossed in the recent past, as well as to establish a time limit of the validity of the current orbital configuration of the system for the longer term simulations.

Next, in order to determine the possible resonant behaviour of Pallene, we performed a set of N-body simulations, spanning from 50 up to 5×10^6 yr of integration time. In this instance, the test particles are not included, and there are only seven bodies orbiting Saturn. The N-body simulations are performed with our implementation of the Implicit integrator with Adaptive time-Stepping of 15th-order (IAS15, Rein & Spiegel 2015) taking into account Saturn's gravitational moments (Table 1). Subsequently, we integrate the satellite system for 50, 5×10^3, 5×10^4, 5×10^5, and 5×10^6 yr. We use the geometric orbital elements to calculate several libration angle combinations, among all satellites in Table 2 and Pallene.

Finally, we study the evolution of the diffuse ring through two distinct scenarios: (a) particles initially co-orbital to the satellite and (b) by considering the temporal evolution of particles launched from Pallene's surface. The study is performed considering the system's gravitational effects and also non-gravitational forces acting in the region, such as solar radiation force, plasma drag, and the electromagnetic force. Using an adapted version of the MERCURY6 package which includes the effects of these forces and Saturn's gravitational moments, we integrated the system formed by Pallene, the six large moons, and a set of 5000 test particles until all the particles were removed from the simulation.

3 PALLENE'S CURRENT DYNAMICAL CONTEXT

3.1 Characterization through frequency map analysis

To gain a better understanding of the dynamical behaviour and future stability of Pallene, as well as of the micrometric dust particles in its vicinity, we carried out a frequency map analysis (Laskar 1990; Laskar, Froeschlé & Celletti 1992; Robutel & Laskar 2001) of a broad region of the geometric a–e phase space plane, surrounding Pallene. We performed a short-term numerical integration (of ∼18 yr, or approximately 5700 Pallene orbital periods and 2000 orbital periods of the most external particle in the map). We used this time span since at least 2000 revolutions of each particle are required to confidently recover the main orbital frequencies.

We included 13 025 test particles distributed in a homogeneous grid covering the a–e geometric plane, with the following conditions: a is sampled from 0.95 to 1.05 $D_{\rm Pal}$ (where $D_{\rm Pal}$ is the normalized average geometric semimajor axis of Pallene) in steps of size $\Delta a = 5 \times 10^{-5}$. In e we sampled from 0 to 0.02 in steps of $\Delta e = 2 \times 10^{-3}$. The remaining orbital elements are all set to zero for simplicity, namely, inclination I, longitude of pericentre ϖ, longitude of the ascending node Ω, and mean anomaly M. We recall that test particles are subject to the gravitational perturbations of an oblate Saturn, Pallene, and the six gravitationally dominant moons in our region of interest.

A frequency analysis for each test particle in the grid was performed, using the algorithm of Šidlichovský & Nesvorný (1996), over the dynamical variable:

$$\xi(t) = a(t)\exp(i\lambda(t)), \tag{1}$$

where $a(t)$ and $\lambda(t)$ are the semimajor axis and mean longitude of each particle, respectively. The variable $\xi(t)$ expresses a combination closely related to a formal combination of the action and angle variables (J_i, η_i), of each orbit, expressed as $\xi_i'(t) = J_i \exp \eta_i$. Though it is clear that $\xi(t)$ and $\xi^{'}(t)$ are not equal, they are still related as $\xi(t) = f(\xi_1', \xi_2', ..., \xi_n')$, f being a function close to unity (Laskar 1993).

When we perform a frequency analysis of $\xi(t)$, we obtain a decomposition of the form

$$\xi(t) = \alpha_0 \exp(i\beta_0) + \sum_{k=1}^{N} \alpha_k \exp(i\beta_k). \tag{2}$$

For a Keplerian orbit, the decomposition of $\xi(t)$ would have only one term, i.e. $\alpha_0 = a$ and $\beta_0 = n$, where β_0 is what we call the 'mean frequency', while a and n are the semimajor axis and mean motion of the particle, respectively. For non-Keplerian orbits, the decomposition given in equation (2) contains many periodic terms. None the less, frequency analysis ensures that if a particle remains in a stable orbit, the conditions expressed by the approximations $\alpha_0 \approx a$ and $\beta_0 \approx n$ will prevail; also, for stable orbits $\alpha_0 \gg \alpha_k$. These conditions do not hold for particles following unstable orbits, for which β_0 will change dramatically from one time interval to the next, since the evolution of chaotic orbits does not remain on the surface of KAM tori.

To compute the change of the main frequencies, we perform a frequency analysis of $\xi(t)$ in two adjacent time intervals of length T, equal to half the total integration time. We call β_{01} and β_{02} the main frequencies obtained in each interval, respectively. Finally, we define a diffusion parameter, D, which provides a measure of the stability of the orbits. Following Correia et al. (2005) and Muñoz-Gutiérrez & Giuliatti Winter (2017), we have

$$D = \frac{|\beta_{01} - \beta_{02}|}{T}. \tag{3}$$

It can be seen that small values of D will be obtained for stable trajectories, while larger values of D are the result of unstable orbital evolution.

3.2 Diffusion map of Pallene's neighbourhood

A diffusion map for the region around Pallene, shown in Fig. 1, was obtained after applying the above procedure to all the grid particles covering the geometric a–e plane. A coloured rectangle is plotted for each particle according to its initial location in the plane, where colour is scaled according to the value of the logarithm of D. Redder colours indicate more unstable orbits, while bluer colours represent the more stable trajectories. Particles that are lost from the simulation before it finished, mainly due to collisions with Pallene, are coloured white. The solid black lines delimit Pallene's collision region, i.e. the region in which, at their apocentric or pericentric excursions, particles will cross Pallene's orbit, thus having a higher probability of colliding with the small moon.

The diffusion map provides a quick method to globally characterize the dynamical state of a vast region of phase-space, at a low computational cost, i.e. using only short-term numerical simulations. Unstable regions are immediately highlighted by the colour contrast. We can quickly identify MMRs, as well as their relative strength. The

Downloaded from https://academic.oup.com/mnras/article/511/3/4202/6462913 by INIST-CNRS INSU user on 20 April 2023

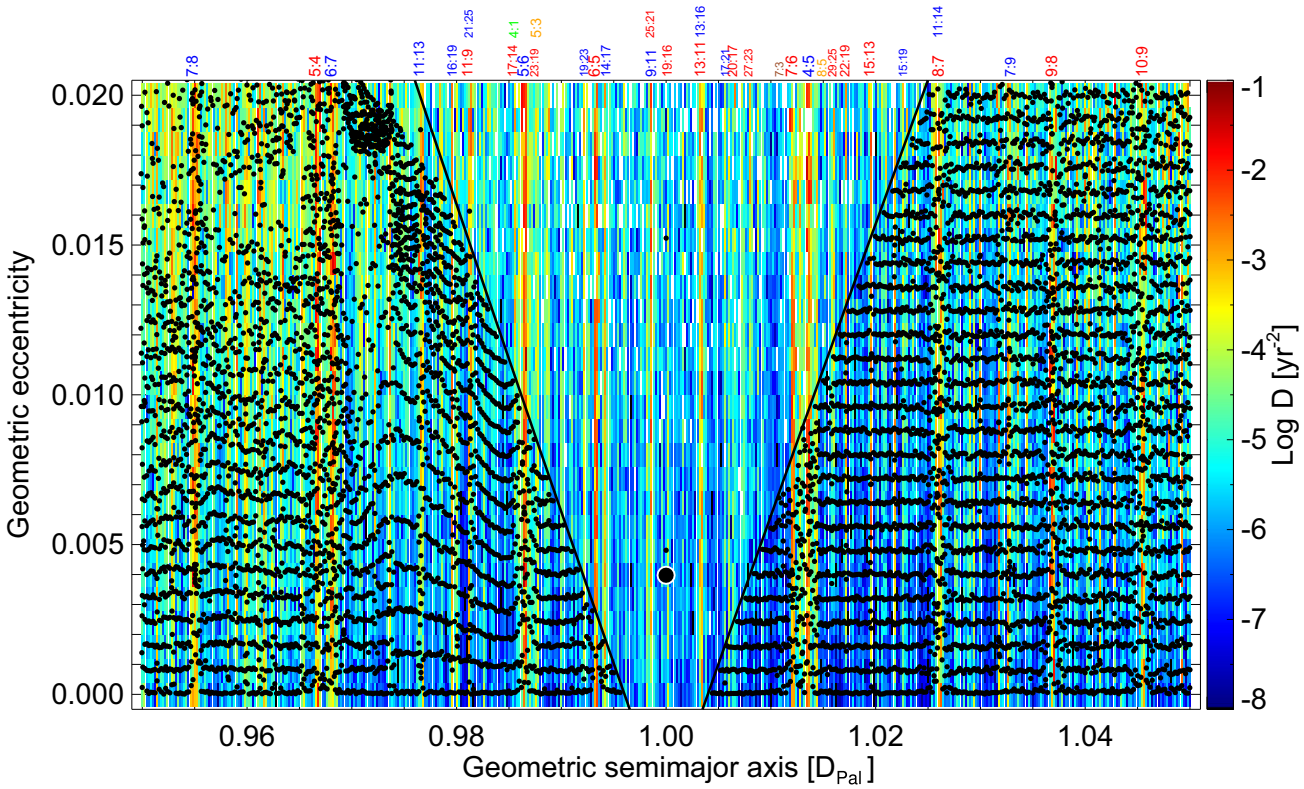


Figure 1. Diffusion map for a wide region of the geometric semimajor axis – eccentricity phase-space plane around Pallene. A colour scale indicates the stability of orbits, where bluer regions represent the more stable, and redder ones the more unstable. Locations where particles were ejected or collided with Pallene before the end of the simulation are coloured in white. The solid black lines stand for the constant pericentre and apocentre distances of Pallene, delimiting the collision region of the small moon. All the MMR ratios which were explored for libration in the simulations of Section 4.2, going from first to fourth order, are labelled at the top of the figure. Colours correspond to MMRs with Mimas (blue), Enceladus (red), Tethys (orange), Dione (brown), and Rhea (green). The final conditions of a longer simulation (10^4 yr), of the same particles used to create the diffusion map, are overplotted on the map (black dots) to highlight the predictive power of the frequency analysis technique for the characterization of the dynamical stability of wide regions of phase space.

semimajor axis parameter space from 0.98 to 1.02 $D_{\rm Pal}$ encompasses completely both Pallene's orbit and the co-orbital dusty ring. In this region the strongest MMRs are due to first-order commensurabilities with either Mimas or Enceladus, however, higher order MMRs with Dione, Tethys, and Rhea can also be observed. The location of all the existing commensurabilities with the six major moons (up to order 4 and degree 30) are indicated at the top of Fig. 1; outside this interval we only indicate the location of first-order MMRs with Mimas and Enceladus. The stronger resonances are characterized by thin vertical structures of homogeneous yellow to orange colour, such as the 4:5, 5:6, 6:7, and 7:8 MMRs with Mimas (blue labels), as well as the 5:4, 6:5, 7:6, 8:7, 9:8, and 10:9 with Enceladus (red labels). Second-, third-, and fourth-order MMR bands are thinner than first-order resonances. Furthermore, MMR chords are less stable than the broader, non-resonant, blue bands, regardless of eccentricity. Aside from possible exceptions at MMRs, lower eccentricity orbits are far more stable in general throughout the map.

From Fig. 1, it is apparent that Pallene, whose location is indicated by the large black circle, is not currently trapped inside any strong MMR, despite the very close proximity of three resonances: the 9:11 with Mimas and the 19:16 and 25:21 with Enceladus.

Moreover, two interesting regions stand out from the map, corresponding to the clustering of several MMRs with various moons. The first of such regions, b_1, is located at ∼0.986 $D_{\rm Pal}$, where the 5:6 MMR with Mimas, the 17:14 and 23:19 MMRs with Enceladus, the 5:3 MMR with Tethys (orange label), and the 4:1 MMR with Rhea (green label) lie in close proximity to each other. The second region, b_2, is located around ∼1.014 $D_{\rm Pal}$; in this region two first-order resonances, the 4:5 with Mimas and the 7:6 with Enceladus, are in close proximity to the 8:5 MMR with Tethys (orange label), and the 7:3 MMR with Dione. It is apparent that the interaction of several low-order resonances results in especially unstable regions at these locations. A similar case occurs at ∼0.966 $D_{\rm Pal}$, where the two first-order resonances, 6:7 with Mimas and 5:4 with Enceladus, produce a particularly wide unstable region.

To reassess the predictive power of the frequency analysis technique, we integrated up to 10 000 yr the same set of 13 025 particles of the grid covering the geometric a–e phase-space plane. The final conditions of this simulation were overplotted on the diffusion map of Fig. 1 with black dots.

To the left of the collision region of Pallene, the largest perturbations in eccentricity are observed for particles located in the bands of MMRs, as expected. The most unstable region, however, is the one located in the top left corner of the map, roughly above 0.015 in eccentricity and to the left of the 11:13 MMR with Mimas; here the direct influence of Mimas is stronger and particles are removed faster. To the right of the collision region, all the particles remain nearly unperturbed, except for the b_2 band where several resonances converge, as well as at the locations of other first-order MMRs with Mimas and Enceladus.

Notably, inside the collision region of Pallene, only three particles survive after 10 kyr, one of them is a co-orbital with the small moon;

Downloaded from https://academic.oup.com/mnras/article/511/3/4202/6462913 by INIST-CNRS INSU user on 20 April 2023

a second lies at the location of the 19:16 MMR with Enceladus, and the last one lies inside the band of the 11:9 MMR with Enceladus, which overlaps with the 21:25 MMR with Mimas.

Both the map and the long-term simulation of the particles serve as an indication of the future evolution of large dust particles, with radii larger than ∼30 μm, i.e. those unaffected by non-gravitational forces known to act in this region. Towards the internal zone of the Pallene collision region, even this kind of large particles would be removed (though at times greater than 10 kyr) due to perturbations from Mimas. Exterior to the Pallene collision region, large particles could in principle survive for very long times. This indicates that the Pallene ring would find greater stability towards semimajor axes larger than that of the small moon, increasing the eccentricity of its conforming particles as they find MMR regions with Enceladus. On the other hand, ring-forming particles within the Pallene collision region could survive mainly as co-orbitals; however, with only one co-orbital and two apparently resonant particles surviving in this region in the 10 kyr simulation, we cannot provide quantifiable predictions for the behaviour of the ring, based exclusively on the diffusion map. For a more in-depth analysis of the possible origin of the ring and its future evolution, we performed a large set of detailed simulations, presented in Sections 5.2 and 5.4 of this paper.

4 DYNAMICAL EVOLUTION OF PALLENE IN DIFFERENT TIME-SCALES

4.1 Tidal evolution

To gain an appropriate perspective on the time-scales of Pallene's dynamical evolution, we first look at Pallene's tidal evolution in between Mimas and Enceladus. Although more complex analyses of tidal evolution in the Saturn system have recently been done (e.g. Fuller, Luan & Quataert 2016; Lainey et al. 2020), here we employ a simpler model to gain a general understanding of the context in which Pallene may have evolved. Using equation (4.213) from Murray & Dermott (1999), we can calculate previous semimajor axes

$$a = a_0 \left[1 - \left(\frac{k_2}{Q} \frac{39 M_m R_S^5}{2 a_0^{13/2}} \sqrt{\frac{G}{M_S}} t \right) \right]^{2/13}, \tag{4}$$

assuming that the tidal dissipation mechanism is linear and that Q is frequency-independent.

For our tidal evolution calculations, we take our value for Saturn's Love number, $k_2 = 0.390$, from Lainey et al. (2017). We estimate a quality factor $Q = 2000$ also based on Lainey et al. (2017) and similar to what is used in Ćuk, Dones & Nesvorný (2016), which was based on the earlier work of Lainey et al. (2012), though there is less agreement on this value and it is meant to apply only near the semimajor axes roughly around Mimas and Enceladus. Previous estimates of Q an order of magnitude higher were due to the assumption that Mimas was primordial (Murray & Dermott 1999; Meyer & Wisdom 2008). However, recent studies that argue Saturn's rings and the mid-sized moons are probably young use a Q value in the range we have assumed (Ćuk et al. 2016; Fuller et al. 2016; Lainey et al. 2017; Hesselbrock & Minton 2019; Neveu & Rhoden 2019). Other values for this calculation are given in Tables 1 and 2.

Using these values, we measured the change in semimajor axis with respect to today's semimajor axis value $\frac{\Delta a}{a}$ over the past 5 Myr for Mimas, Pallene, Enceladus, Tethys, and Dione. Out of these measurements, Mimas has $\frac{\Delta a}{a} = 0.0017$, which is the largest among these moons. Because this change in semimajor axis due to tidal evolution is small, we expect our long-term simulations of 5 Myr without the inclusion of tidal evolution to be accurate enough.

From the semimajor axis calculations, if Pallene is old enough, it may have recently escaped the 4:5 resonance with Mimas (40 Myr ago with $Q = 2000$). Prior to escape, Pallene could have migrated with Mimas for a substantial period of time. For this reason, it becomes difficult to project Pallene's previous tidal evolution with much certainty. If Pallene was not captured in any resonance with Mimas for a significant period of time, which is unlikely because their orbits are converging, then further in the past Pallene's orbit may have crossed that of Enceladus (400 Myr ago with $Q = 2000$), suggesting that Pallene could be a fragment from Enceladus, similar to the way Showalter et al. (2019) propose that Hippocamp could have fragmented off of Proteus, possibly from a cometary impact.

Hippocamp is close to the orbit that is synchronous with Neptune's rotation, which, together with the fact that it is the least massive of Neptune's moons, implies that the rest of Neptune's moons are diverging from Hippocamp. In contrast, Pallene's orbit is converging with Mimas's orbit. For this reason, Pallene is expected to have been captured into resonance with Mimas at each resonance crossing, but it is difficult to determine the duration of the capture in each resonance.

Proteus and Hippocamp have mean radii of 203.8 and 17.4 km (Showalter et al. 2019), while Enceladus and Pallene have mean radii of 252 and 2.23 km (Roatsch et al. 2009; Thomas et al. 2013). Using these mean radii and masses of 1.08×10^{20} kg for Enceladus (Jacobson et al. 2006) and 4.4×10^{19} kg for Proteus (multiplying the volume from Stooke (1994) by an assumed density of 1.3 g cm^{-3}), the escape velocity $v_{\rm esc} = \sqrt{2GM_m/R_m}$ from the surface of Enceladus is 240 m s^{-1}, while for Proteus it is 170 m s^{-1}. Pallene has a smaller size ratio to Enceladus than Hippocamp has to Proteus, but perhaps Pallene is evidence of the proposed impactor in the south polar terrain of Enceladus (Roberts & Stickle 2017).

Not too long in the past, however, is the Mimas-Enceladus 3:2 resonance crossing (115 Myr ago with $Q = 2000$). Meyer & Wisdom (2008) studied a triplet of Mimas-Enceladus 3:2 resonances and found that Mimas's eccentricity can be explained either by passage through the 3:2 e-Mimas resonance or the 6:4 ee'-mixed resonance (but not the 3:2 e-Enceladus resonance), and found dynamical escape to be possible for both of these resonances. Ćuk et al. (2016) proposed that Tethys, Dione, and Rhea all formed in one event about 100 Myr ago, and suggests that Mimas and Enceladus could have formed during the same epoch or could be even younger. Neveu & Rhoden (2019), however, have suggested that Mimas could be significantly younger than Enceladus. This last scenario allows for the possibility of Pallene migrating away from Enceladus after an impact before the formation of Mimas.

Thus, given a constant Q tidal model, it looks like Pallene has crossed some resonances, which, especially if it had been trapped in any of them for some period of time, could have affected its eccentricity and inclination. However, the new tidal models indicate the evolution of the satellites could be more complex than previously thought (Fuller et al. 2016; Lainey et al. 2020). Still, small moons such as Pallene are likely sensitive probes of this tidal evolution (see, for example, El Moutamid, Sicardy & Renner 2017) and so should be considered in those contexts.

4.2 Resonance analysis

In view of the rich dynamical structure of the phase-space close to Pallene, where many resonances are in close proximity to each other, we seek to determine whether any particular resonance between Pallene and one or more of the major Saturnian moons drives

Downloaded from https://academic.oup.com/mnras/article/511/3/4202/6462913 by INIST-CNRS INSU user on 20 April 2023

Table 3. Order k and degree j explored for libration angles with Pallene.

Moon	k	j
Mimas	1	5, 6
	2	10–12
	3	15–19
	4	20–25
Enceladus	1	6, 7
	2	11–15
	3	17–22
	4	22–30
Tethys	2	5
	3	8
	4	10
Dione	4	7
Rhea	3	4

the evolution of Pallene, or could be a possible mechanism to confine the particles of the dusty ring. Hence, we ran five sets of numerical N-body simulations with different integration times, i.e. 50 (or approximately 15 766 Pallene's orbits), 5×10^3, 5×10^4, 5×10^5, and 5×10^6 yr. The output interval in each integration is always a multiple of Pallene's orbital period, $P \approx 1.2$ d, so that in each output file there are a total of 15 220 data points. For each integration, several libration angles from the direct and indirect arguments of the disturbing function were explored, up to fourth-order (Murray & Dermott 1999). Due to the uncertainties in Pallene's density and therefore its mass, three different densities were considered as described in Section 2, which means that in total 15 realizations were performed, three per each integration time; we designate these as density-sets per integration time.

We referred to the resonant arguments of the disturbing function for two reasons: (1) the number of possible arguments is constrained and (2) in the case that one of these arguments librates, then the corresponding argument would facilitate its use in future secular theory calculations of this system. The libration angle among an outer (with primed orbital elements) and an inner satellite (un-primed elements) is expressed as

$$\phi = j\lambda' + (k - j)\lambda + \gamma(\varpi', \varpi, \Omega', \Omega), \tag{5}$$

where k is the order, j the degree, and γ is a linear combination of ϖ', ϖ, Ω', and Ω. The examined libration angles range in order k from 1 to 4, while the degree j corresponds to possible resonances within 0.98 and 1.02 $D_{\rm Pal}$. The linear combination $\gamma(\varpi', \varpi, \Omega', \Omega)$ in equation (5) is determined from the direct and indirect arguments of the disturbing function described in Murray & Dermott (1999), which have the form $\gamma = k_1\varpi' + k_2\varpi + k_3\Omega' + k_4\Omega$, where $k_1 + k_2 + k_3 + k_4 = k$.

In the rest of this section, we denote the libration angles of a given moon with Pallene by their capitalized initials, e.g. $\phi_{\rm PM}$ for the Pallene-Mimas libration angle, except for Tethys which will be denoted by a 't' to distinguish it from Titan. For the semimajor axis interval considered above, the possible resonant combinations are summarized in Table 3. The majority of explored direct arguments involve either Pallene and Mimas, or Pallene and Enceladus. In contrast, the combination between Pallene and Titan lacks possible resonant combinations in this semimajor axis interval. For completeness, additional zeroth-order resonances were also evaluated for degrees $j = 0$ to 15.

We inspected 75 indirect arguments per moon pair, i.e. 450 in total, denominated as ψ to distinguish them from the direct arguments, ϕ. Most of the indirect arguments explore all the angular range in

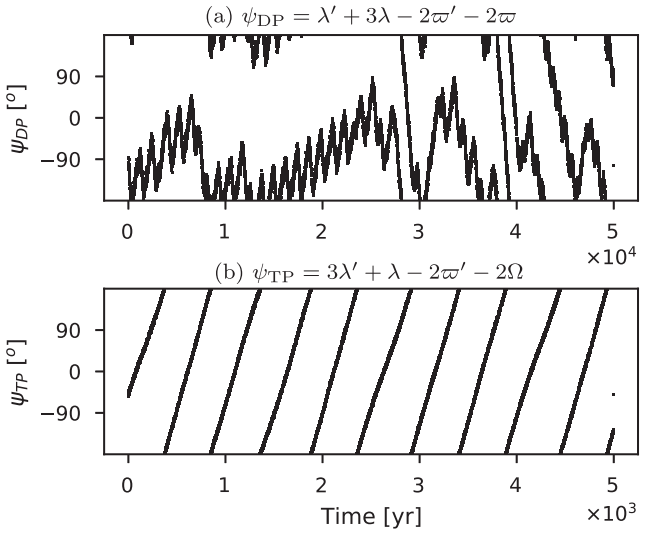


Figure 2. Unique indirect arguments in our search with either librating properties or long-period circulation. The remaining 448 arguments displayed short-period circulation.

every time-scale. Only two fourth-order indirect arguments show interesting behaviour: the Dione-Pallene argument $\psi_{\rm DP} = \lambda' + 3\lambda - 2\varpi' - 2\varpi$ displays temporal libration (Fig. 2a) for about 30 kyr, while the Titan-Pallene argument $\psi_{\rm TP} = 3\lambda' + \lambda - 2\varpi' - 2\Omega$ (Fig. 2b) presents a long circulation period of 494 yr.

In contrast, the direct arguments displayed a broader variety of phenomena depending on the time-scale of the integration: circulation, alternating intervals of circulation, libration, or overall circulation with 'steps' of near constant value. In Sections 4.3 and 4.4, we only present angles that show resonant-like features and that coincide within a given density-set; we display the evolution of $\rho_{\rm Pal} = 0.25$ g cm^{-3} integrations only. Nevertheless, when the resonant-like libration angles are compared within density-sets, we find that for integrations longer than 5×10^3 yr the angles evolve similarly within 5×10^4 yr but differ after this threshold. Consequently, the effect of Pallene's mass in its dynamical evolution is small and only noticeable after 10^4 yr or $\sim 10^6$ Pallene orbits.

We divide our analysis into short-term (50 yr) and long-term ($t \geq 5 \times 10^3$ yr), demonstrating that Pallene has different resonant behaviour with one or more Saturnian satellites depending on the time-scale, some emerging just in either short- or long-term simulations.

4.3 Short-term evolution of direct arguments

The intention of the 50 yr simulations was to re-examine the suggested third-order resonance between Pallene and Enceladus (Spitale et al. 2006). We probed for libration all 10 possible direct arguments with $19\lambda' - 16\lambda$, finding one additional combination with interesting behaviour in this interval. Fig. 3 shows a comparison between the resonant angle suggested by Spitale et al. (2006) (Fig. 3a) and our finding (Fig. 3b). The angle $\phi_{\rm EP} = 19\lambda' - 16\lambda - \varpi - 2\Omega$, circulates with a period of 10.6 yr. Similarly, Muñoz-Gutiérrez & Giuliatti Winter (2017) found this angle to circulate but with a period 1.8 times shorter. The angle $\phi_{\rm EP} = 19\lambda' - 16\lambda - \varpi' - 2\Omega'$ differs from that suggested in Spitale et al., in that the longitudes of ascending node and pericentre belong to the outer satellite instead of the inner one. The evolution of this argument exhibits a softer negative slope that circulates with a period of ~30 yr.

Downloaded from https://academic.oup.com/mnras/article/511/3/4202/6462913 by INIST-CNRS INSU user on 20 April 2023

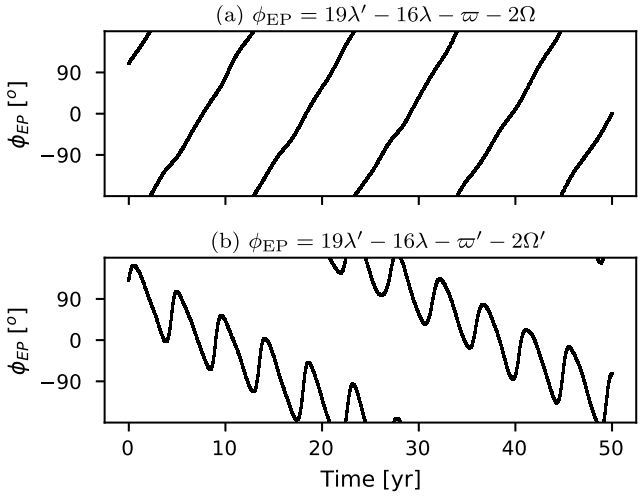


Figure 3. Two different 19:16 libration angles between Enceladus and Pallene over 50 yr. The top panel corresponds to the resonant angle suggested by Spitale et al. (2006) and the bottom panel corresponds to our finding. Although both libration angles circulate, the argument in Fig. 3(b) has a circulation period three times longer than the one in Fig. 3(a).

In contrast to other small moons in the region, clearly trapped in first-order MMRs with Mimas, such as Aegaeon in the 7:6 (Hedman et al. 2010; Madeira et al. 2018), Methone in the 14:15 (Spitale et al. 2006; Hedman et al. 2009; Callegari, Rodríguez & Ceccatto 2021), and Anthe in the 10:11 (Cooper et al. 2008; Callegari & Yokoyama 2020), our short-term (and long-term) simulations indicate that Pallene's evolution is not characterized uniquely by any MMR, either with Mimas or Enceladus. Although some of the 19:16 libration angles between Pallene and Enceladus present features associated with a near-resonance, they all clearly circulate in longer time-scales. It is likely that Pallene is just outside the parameter space that characterizes the 19:16 MMR with Enceladus. Similarly, several of the libration angles shown outside of the Mimas-Anthe 10:11 MMR (fig. 8 in Callegari & Yokoyama 2020) resemble the evolution of some of the direct arguments we studied in this work. The latter suggests that an analysis of the 'individual dynamic power spectra' (IPS in Callegari & Yokoyama 2020) of the 19:16 MMR between Pallene and Enceladus could disclose the nature of the current resonant state of Pallene (Fig. 3), however, we consider such analysis beyond the scope of this work.

4.3.1 Simultaneous zeroth-order direct argument among all moons

While examining the zeroth-order direct arguments of the 50 yr simulations, a simultaneous resonant libration angle was detected between Pallene and four other moons: Mimas, Tethys, Dione, and Titan. Here, 'simultaneous' means that more than one pair of satellites (Pallene and another large Saturnian moon) displays apparent resonant properties for the same libration angle expression. In this case, this simultaneity emerged for $\Phi \equiv \varpi^{'} - \varpi + \Omega^{'} - \Omega$ as presented in Fig. 4. In this time interval, Φ appears to be constant with small oscillations, except for the pairs Enceladus–Pallene and Rhea–Pallene, which circulate with a period of 12 and 36 yr, respectively. None the less, Enceladus displays a semiresonant behaviour due to the step-like oscillation of $\Phi_{\rm EP}$. Each 'step' has a semiconstant value that changes in each full circulation. For example, in the first step (from 1 to 4 yr) the nearly constant value is 90° and on the fourth step (from 14 to 18 yr) the corresponding value is 60°; therefore, there

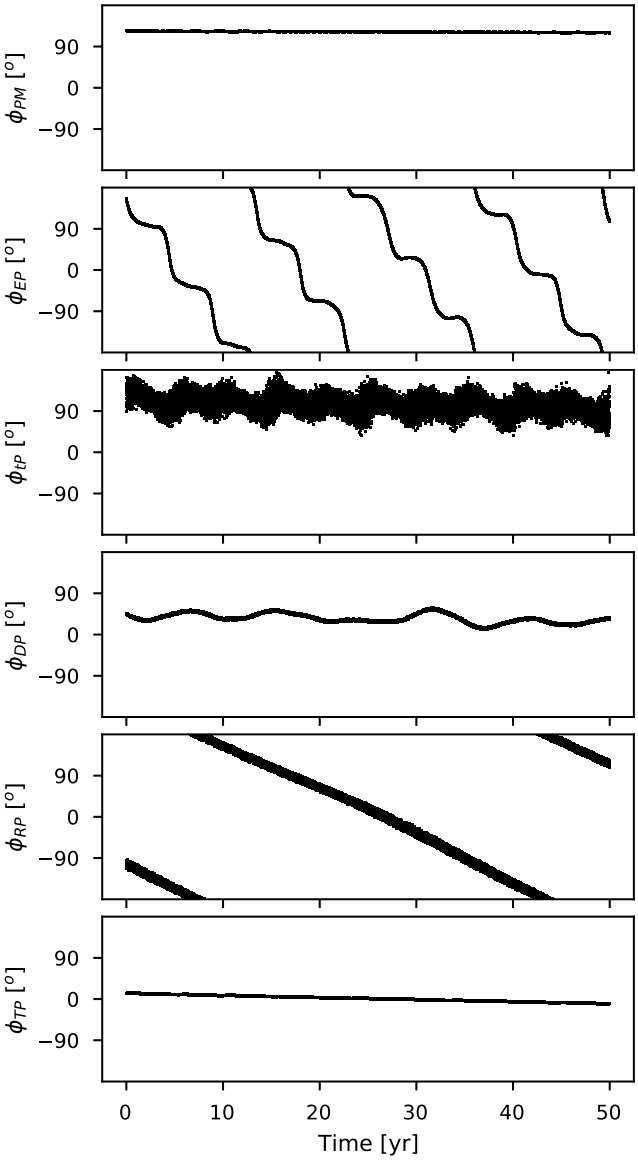


Figure 4. 50 yr evolution of the libration angle $\Phi = \varpi^{'} - \varpi + \Omega^{'} - \Omega$ between each moon in Table 2 and Pallene. The known libration angle between Pallene and Mimas (Callegari & Yokoyama 2010, top panel) also presents resonant behaviour between Pallene and three other moons: Tethys, Dione, and Titan (third, fourth, and sixth panels from top to bottom). In contrast, $\Phi_{\rm EP}$ exhibits circulation with semiconstant 'steps', whereas $\Phi_{\rm RP}$ (fifth panel) circulates.

are ∼4 yr intervals where this angle librates followed by a shift of ∼130° during ∼1.5 yr to another semiconstant step.

Callegari & Yokoyama (2010) suggested this quasi-resonant relationship between Mimas and Pallene ($\Phi_{\rm PM}$) and demonstrated that it has a long circulation period (∼5000 yr, later confirmed by Muñoz-Gutiérrez & Giuliatti Winter 2017)). In order to explore possible circulation of Φ for Tethys, Dione, and Titan, we looked for circulation of this direct argument in our 5×10^3 yr integrations and, if circulation existed, determined the corresponding period using Fourier frequency analysis. Table 4 lists the circulation periods of Φ for each moon pair, including our estimate for $\Phi_{\rm PM} = 4708$ yr. The measured circulation periods for Tethys–Pallene (tP), Dione–Pallene (DP), and Titan–Pallene (TP), are 872, 844, and 794 yr,

Downloaded from https://academic.oup.com/mnras/article/511/3/4202/6462913 by INIST-CNRS INSU user on 20 April 2023

Table 4. Period of libration angle $\phi = \varpi' - \varpi + \Omega' - \Omega$ for the moon pairs in Fig. 4.

Moon pair	$P_{\rm circ}$ [yr]	No. orbits [10^3]
PM	4708	1495.5
EP	12	3.9
tP	872	277.0
DP	844	268.2
RP	36	11.3
TP	794	252.4

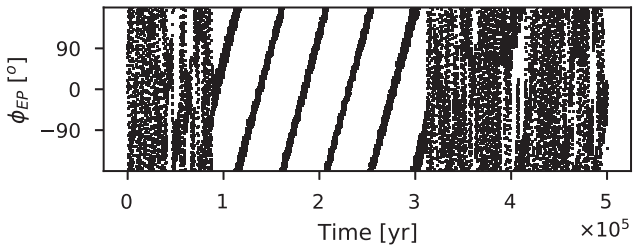


Figure 5. First-order argument $\phi_{\rm EP} = 7\lambda' - 6\lambda + \varpi - 2\Omega$ between Enceladus and Pallene over 5×10^5 yr. A change in the circulation frequency is observed between 100 to 300 kyr.

respectively. Even though these angles are not resonant, their long circulation relative to Pallene's orbital period might significantly affect the dynamics of Pallene in the short term.

The possible existence of a quasi-resonance with the same combination of angles that excludes the mean longitudes suggests an alignment of the lines of nodes and apses of Pallene, Mimas, Tethys, and Dione, most likely with Titan. In other terms, a combination of the eccentricity and inclination vectors of these satellites may be aligned to some extent to Titan's. This is not entirely unexpected, since secular resonances could lead to apsidal alignments; in the Saturnian system an example of this has long been known to occur between Rhea and Titan (see Greenberg 1975, and references therein). The well-known example of Tethys–Mimas 2:4 MMR ($\phi_{\rm tM} = 4\lambda' - 2\lambda - \Omega' - \Omega$), for which the variation in inclination drives the resonance (Allan 1969; Greenberg 1973), is another important example of node alignment. Moreover, alignment of the nodes has been discussed in several works involving the dynamics of compact extrasolar systems (e.g. Kaib, Raymond & Duncan 2011; Boué & Fabrycky 2014; Granados Contreras & Boley 2018); the later works refer to this alignment as the interaction of an outer massive planet/companion with an inner compact system (of planets) which affects the inner system as if it were a rigid body. In the case of the Saturnian moon system, a study of the compactness of the orbits interior to Titan could reveal whether this phenomenon also occurs in this system. None the less, a detailed study of this scenario is currently beyond the scope of this paper focused on Pallene dynamics; thus we consider this idea for future work.

4.4 Long-term evolution of direct terms

We performed four long-term simulations, lasting 5×10^3, 5×10^4, 5×10^5, and 5×10^6 yr. In these simulations, most of the explored arguments circulate. Although a handful of angles display resonant characteristics during definite time intervals, there is not a single case

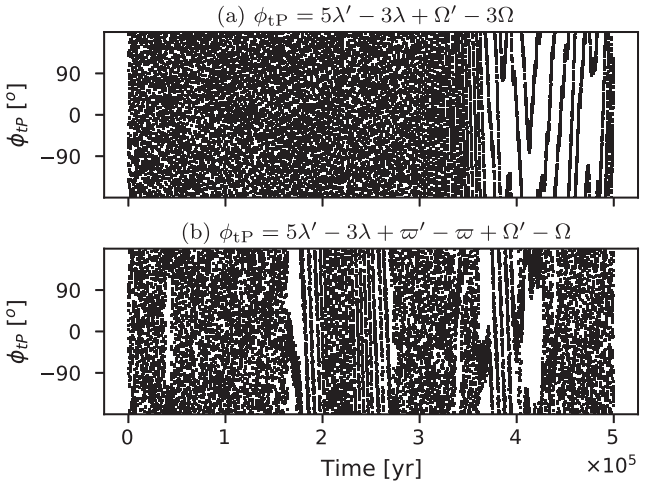


Figure 6. Second-order 5:3 MMR between Tethys and Pallene. Both arguments present temporal libration at different times that last for thousands of years.

in which the libration angle has a constant value for the total length of the simulations.

In Sections 4.4.1 and 4.4.5, we present libration angles of interest separated by order, at least one per order, from first- to fourth-order finishing with zeroth-order. The second-order arguments in Section 4.4.2 failed to produce similar behaviour among the density-set in all time-scales. However, we include the results of two Tethys–Pallene arguments (each with distinct densities for Pallene) displaying temporal libration to exemplify the long-term effect of Pallene's mass in determining its resonant state.

4.4.1 *First-order arguments*

Only one first-order argument presenting unusual features was recovered from our simulations (Fig. 5). Although it circulates at all times in the 5×10^5 yr integration, this 7:6 argument between Enceladus and Pallene shows a change in circulation frequency that slows down and holds for more than 2×10^5 yr, a considerable interval in terms of Pallene's orbital period. The exact resonance is located at $1.012 D_{\rm Pal}$ and is one of the strongest resonances in the region considered in this work (see map of Fig. 1). However, due to its semimajor axis being far from the 7:6 MMR location, it is unlikely that Pallene would be trapped or suffer strong perturbations from Enceladus through this resonance.

4.4.2 *Second-order arguments*

Fig. 6 presents the evolution of two second-order libration angles with the same degree, 5:3, over 5×10^5 yr. The argument involving the longitudes of ascending nodes of Tethys and Pallene (6a), corresponding to the simulation with $\rho_{\rm Pal} = 0.19\ {\rm g\,cm^{-3}}$, exhibits two librating intervals, one between 350 and 400 kyr and another extending from 450 to 500 kyr, with a slow circulation period enclosed by both intervals. On the other hand, the second argument (6b) is an outcome of the $\rho_{\rm Pal} = 0.34\ {\rm g\,cm^{-3}}$ simulation and involves both the nodal and apsidal longitudes. This argument briefly librates at different intervals of the simulation, the most notable of which covers the 400 to 450 kyr interval.

Downloaded from https://academic.oup.com/mnras/article/511/3/4202/6462913 by INIST-CNRS INSU user on 20 April 2023

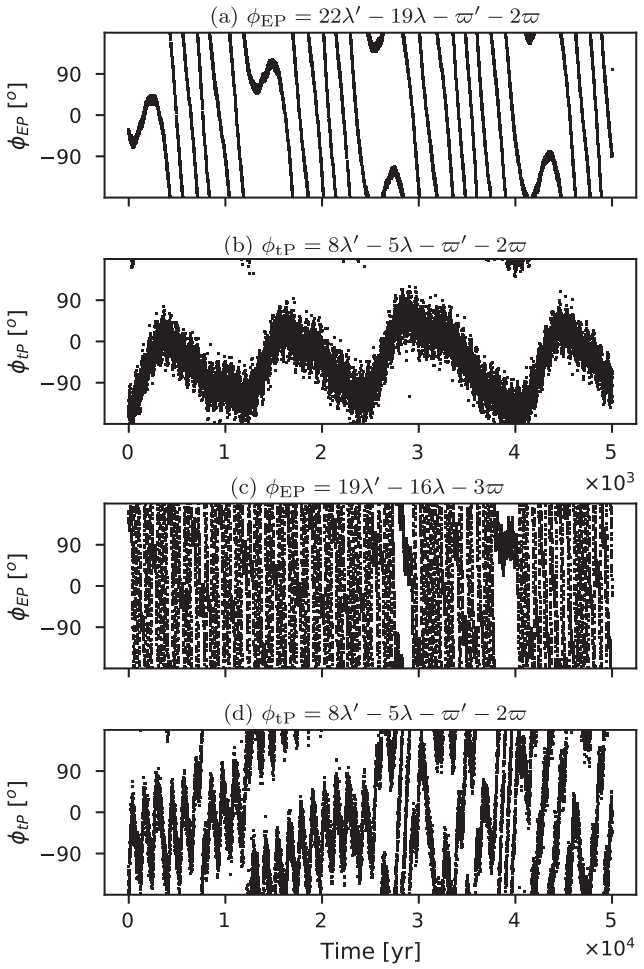


Figure 7. Third-order direct arguments between Enceladus and Pallene and between Tethys and Pallene on different time-scales. From all the arguments with librating properties, the argument $\phi_{\rm tP} = 8\lambda^{'} - 5\lambda - \varpi^{'} - 2\varpi$ (Figs 7b and d) librates for about 10 kyr, the longest time amongst our findings in Section 4.

4.4.3 *Third-order arguments*

In total, three different third-order arguments were found (Fig. 7), associated with resonances with Enceladus and with Tethys. On the 5×10^3 yr time-scale, the direct argument $\phi_{\rm EP} = 22\lambda^{'} - 19\lambda - \varpi^{'} - 2\varpi$ between Enceladus and Pallene (Fig. 7a) circulates for most of the integration yet displays intervals of libration which last about 400 yr, and, similar to the argument in Fig. 5, shifts the constant value at which it librates, e.g. in the first 400 yr it librates close to 0° and then shifts to librate close to 90° from the 1200 to 1600 yr interval. The argument associated with the 8:5 MMR between Tethys and Pallene, $\phi_{\rm tP} = 8\lambda^{'} - 5\lambda - \varpi^{'} - 2\varpi$, exhibits a clear ample libration for the duration of the integration. Fig. 7(b) is the clearest example of libration found in our exhaustive exploration of resonant arguments between Pallene and a major Saturnian moon.

On the 5×10^4 yr realizations (Figs 7c and d), we recover a Tethys–Pallene 8:5 argument and find an additional 19:16 direct argument between Enceladus and Pallene. The latter argument (Fig. 7c), $\phi_{\rm EP} = 19\lambda^{'} - 16\lambda - 3\varpi$, presents a distinct libration interval between 3.8 and 4×10^4 yr around 90°. Finally, the Tethys–Pallene 8:5 argument is displayed in Fig. 7(d). We observe that the soft slope visible in the shorter time-scale (Fig. 7b) is maintained in this scale, which then steepens after $\sim 1.2 \times 10^4$ yr until the argument initiates an erratic behaviour, followed by alternating circulation and libration intervals. Similar behaviour occurs in the 5×10^5 realization, but not in our longest integrations (5×10^6 yr) where the 8:5 argument no longer exhibits signs of libration, just circulation.

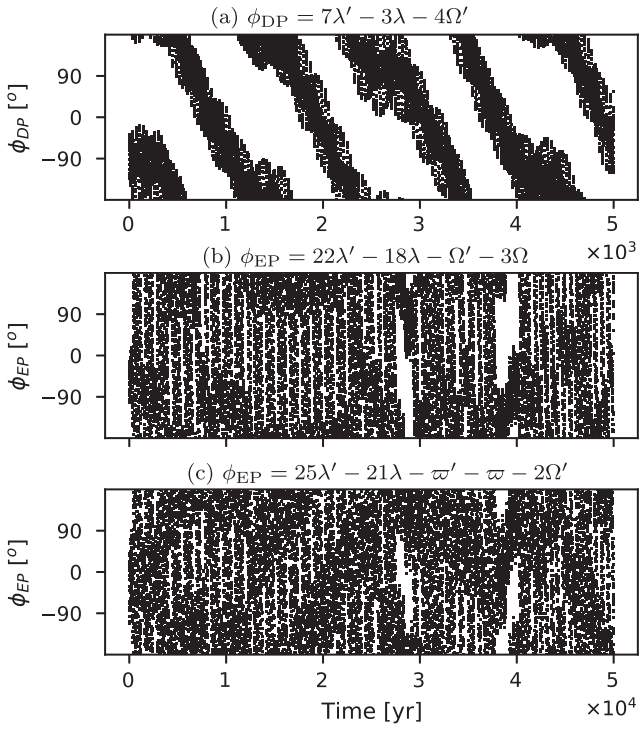


Figure 8. Evolution of fourth-order direct arguments (of Pallene) with Dione and with Enceladus on different time-scales.

4.4.4 *Fourth-order arguments*

We identified three direct arguments of fourth-order with temporal libration with Dione and with Enceladus. Fig. 8(a) illustrates the argument $\phi_{\rm DP} = 7\lambda^{'} - 3\lambda - 4\Omega^{'}$ between Dione and Pallene; this inclination-type resonance involves only the longitude of the ascending node of Dione; it was recovered in the time-scale of 5×10^3 yr only. Despite the general circulation of this argument, some libration intervals with large amplitude about 180° are observed.

The remaining arguments are between Enceladus and Pallene (Figs 8b and c) over 5×10^4 yr which have the particularity that they coincide in the location of their temporal libration and have similar width in Fig. 1. The argument $\phi_{\rm EP} = 22\lambda^{'} - 18\lambda - \Omega^{'} - 3\Omega$ corresponds to the Enceladus–Pallene 11:9 MMR location in Fig. 1, while the argument in Fig. 8(c), i.e. $\phi_{\rm EP} = 25\lambda^{'} - 21\lambda - \varpi^{'} - \varpi - 2\Omega^{'}$, is situated at 0.9983 $D_{\rm Pal}$ almost overlapping the Mimas–Pallene 9:11 MMR.

4.4.5 *Zeroth-order arguments*

We recovered several zeroth-order arguments with various degrees of Pallene with Dione, Rhea, and Titan from the 5×10^4 and 5×10^6 yr integrations. The clearest libration occurs in the argument $\phi_{\rm TP} = 5\lambda^{'} - 5\lambda + \varpi^{'} + \varpi - \Omega^{'} - \Omega$ between Titan and Pallene (Fig. 9c) which coincides with the libration intervals of $\phi_{\rm RP} = 13\lambda^{'} - 13\lambda + \varpi^{'} - \varpi - \Omega^{'} + \Omega$ (Fig. 9b) and the reversal of circulation of $\phi_{\rm DP} = 3\lambda^{'} - 3\lambda + \varpi^{'} + \varpi - 2\Omega^{'}$ (Fig. 9a). A different argument involving

Downloaded from https://academic.oup.com/mnras/article/511/3/4202/6462913 by INIST-CNRS INSU user on 20 April 2023

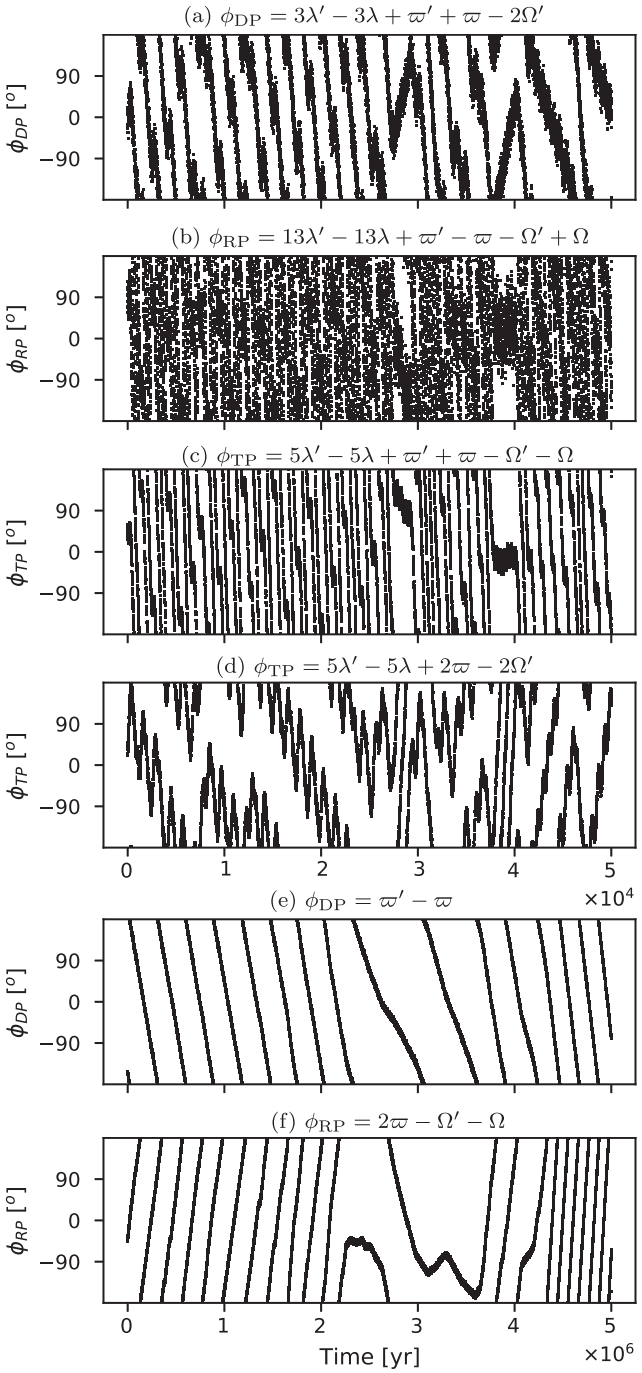


Figure 9. Several zeroth-order arguments over time-scales of 10^4 and 10^6 yr. In these time-scales, none of the zeroth-order arguments repeat as in Section 4.3.1. Furthermore, two Titan–Pallene direct arguments of degree 5 were recovered (Figs 9c and d); the latter displays a clearer temporal libration about 0° at 3.75×10^4 yr.

Titan and Pallene also with degree 5 is shown in Fig. 9(d). It displays a slow circulation with intervals of faster circulation coincident with the libration period of the argument in Fig. 9(c).

Finally, the bottom two panels in Fig. 9 only involve the apsidal and nodal longitudes. The longer and most evident circulation found in our simulations occurs between the longitudes of pericentres of Dione and Pallene (Fig. 9e), while a reversal in the circulation of the argument $\phi_{RP} = 2\varpi - \Omega^{'} - \Omega$ between Rhea and Pallene (Fig. 9f) takes place around 2 and 3 Myr, producing a temporary libration in this interval.

4.5 What all these arguments mean

In our exhaustive search for resonant behaviour, we did not find any clear libration for either first- or second-order resonances among any of the Pallene pairings with the six large moons considered in this work. This means that the proposed 19:16 MMR between Enceladus and Pallene does not exist.

The quasi-resonant zeroth-order argument suggested by Callegari & Yokoyama (2010) between Pallene and Mimas is also present with other moons. Taking into account the values of e and I, we consider that the most important contribution of this combination to the disturbing function would be the one arising from the Mimas–Pallene pair, followed by the Titan–Pallene pair. The small discrepancy in the circulation period found in this paper with respect to the value found in Muñoz-Gutiérrez & Giuliatti Winter (2017) may be due to the updated values of both GM_m and Saturn's zonal harmonics.

The clearest librations, observed for arguments of third- and fourth-order resonances, would, however, have only a slight contribution to the disturbing function, given the small eccentricities and inclinations of both Pallene and the other moons. For the same reason, we do not expect that any resonance of major order, or with the same order but of a larger degree, would result in any significant contribution to the evolution of Pallene.

Based on our analysis, we can conclude that Pallene is not currently trapped in any two-body MMR of any order or degree. This does not exclude the possibility of the existence of a more complex, three-body resonance, involving Pallene and some of the other moons, not exclusive to Mimas and Enceladus. Although a preliminary analysis of this possibility does not show any clear signs for the existence of such a configuration, an in-depth analysis of three-body resonances is left for future work.

We find no significant variations in the overall results of simulations shorter than $\sim 2 \times 10^4$ yr as a function of density (this includes all the simulations referring to the evolution of Pallene's ring). For longer simulations, the accumulation of numerical errors, resulting from differences in the GM_m values of order 10^{-7}–10^{-8}, and the weak chaotic nature of the N-body problem, leads to a loss of coherence among different simulations; none the less, statistically, all the longer term simulations are equivalent to each other up to our longest integration time of 5×10^6 yr. Despite the shift in angular phases, the main orbital elements, (a, e, I), remain confined and evolve regularly up to 5 Myr.

5 ORIGIN AND DYNAMICAL EVOLUTION OF THE PALLENE RING

Pallene shares its orbit with a complete dusty ringlet (Hedman et al. 2009, 2010) seen by *Cassini* images in high phase angle, while a concentration of large particles ($\gtrsim$100 μm) was detected in other phase angle images (Hedman et al. 2009). These data indicate that the ring is composed of micrometre-sized particles and denser bodies. Hedman et al. (2009) found that the ring has a radial full width of ∼2500 km and a vertical profile with a full width at half-maximum (FWHM) of ∼50 km, that is, the ring is vertically thin. More recently, Spahn et al. (2019) measured the FWHM of the Gaussian vertical profile as ∼270 km while obtaining the same radial full width as

Downloaded from https://academic.oup.com/mnras/article/511/3/4202/6462913 by INIST-CNRS INSU user on 20 April 2023

Hedman et al. (2009). Spahn et al. (2019) also found that the radial mean position of the ring is shifted radially outwards by ∼1100 km.

5.1 Pallene's mass production by impacts

In theory, satellites of a few kilometres in radius are efficient sources of debris for rings and arcs due to their reasonably large cross-section and low escape velocity (Poppe 2016). However, Madeira et al. (2018, hereafter M18) and Madeira & Giuliatti Winter (2020, hereafter M20) found that Saturn's three smallest moons (Aegaeon, Anthe, and Methone) do not replenish the material lost by their associated arcs due to non-gravitational forces. It raises the question of whether Pallene can maintain its diffuse ring in a steady state, as proposed by Hedman et al. (2009). In this section, we compute the amount of debris ejected from Pallene and analyse the fate of the ejecta in Section 5.4.

The production of material by Pallene is the result of energetic collisions between the surface of the satellite and fluxes and interplanetary dust projectiles (IDPs) (Grun et al. 1985; Divine 1993). Typically, IDPs are supplied by families of comets (Jupiter-family, Halley-type, and Oort-Cloud comets, Dikarev et al. 2005; Nesvorný et al. 2010; Poppe, James & Horányi 2011) and by the Edgeworth–Kuiper Belt (EKB, Landgraf et al. 2002). Data obtained by the Student Dust Counter (SDC) on-board the New Horizons spacecraft indicate that the Saturn neighbourhood is dominated by EKB dust (Piquette et al. 2019; Poppe et al. 2019) corresponding to the population that reaches the orbits of Saturn's satellites.

In addition to the impacts with IDPs, Pallene may produce material due to impacts with the E ring particles (ERPs). The icy-dust emission from Enceladus's volcanism is the principal source of the E ring (Spahn et al. 2006; Kempf, Beckmann & Schmidt 2010), producing a dense debris that impacts the surface of satellites immersed in the E ring (Spahn et al. 2006). The mass production rate by Pallene (or any other satellite) is given by (Krivov et al. 2003):

$$M^{+} = \pi R_m^2 (F_{\rm IDP} Y_{\rm IDP} + F_{\rm ERP} Y_{\rm ERP}), \tag{6}$$

where R_m is the satellite radius, $F_{\rm IDP}$ and $F_{\rm ERP}$ are the mass flux of impactors due to IDPs and ERPs, respectively, and $Y_{\rm IDP}$ and $Y_{\rm ERP}$ are the ejecta yields associated with each projectile-type.

The ejecta yield is the ratio between the mass produced during the impact and the impactor's mass. This quantity is calculated using the empirical prescription obtained by Koschny & Grün (2001) for pure-ice satellites:

$$Y = \frac{6.69\times10^{-8}}{2^{1.23}\,\mathrm{kg\,m^{-3}}} \left(\frac{1}{927\,\mathrm{kg\,m^{-3}}}\right)^{-1} \left(\frac{m_{\rm imp}}{\mathrm{kg}}\right)^{0.23} \left(\frac{v_{\rm imp}}{\mathrm{m\,s^{-1}}}\right)^{2.46}, \tag{7}$$

where $m_{\rm imp}$ and $v_{\rm imp}$ are the mass and velocity of the impactor.

Pallene, Aegaeon, Anthe, and Methone are likely porous satellites (Hedman et al. 2020), due to their bulk densities, ρ_m, being lower than the density of ice ($\rho_{\rm ice} = 927\,\mathrm{kg\,m^{-3}}$). Since an impact on a porous body is expected to generate more material than an impact on a non-porous surface, we artificially modified equation (7) by introducing a porosity ratio of $\alpha_{\rm p} = \rho_{\rm m}/\rho_{\rm ice}$:

$$Y_p = \frac{(6.69\times10^{-8})^{\alpha_p}}{2^{1.23}\,\mathrm{kg\,m^{-3}}} \left(\frac{\alpha_p}{927\,\mathrm{kg\,m^{-3}}}\right)^{-1} \left(\frac{m_{\rm imp}}{\mathrm{kg}}\right)^{0.23} \left(\frac{v_{\rm imp}}{\mathrm{m\,s^{-1}}}\right)^{2.46}. \tag{8}$$

We must point out that equation (8) is theoretical, and there is no experimental evidence that it actually rules the yield for a porous body. In this work, we will use equation (8) only as an artifice to demonstrate the uncertainties related to the collision yield. The parameters assumed for the two projectile populations are presented below.

5.1.1 *Interplanetary dust projectiles*

In Saturn's vicinity, the (unfocused) IDP mass flux is estimated to be $F_{\rm IDP}^{(\infty)} = 10^{-16}\,\mathrm{kg\,m^{-2}\,s^{-1}}$ (Altobelli et al. 2018; Piquette 2019). We assume the IDPs' velocity near Saturn as the median speed of EKB grains, $v_{\rm imp}^{(\infty)} = 3.1\,\mathrm{km\,s^{-1}}$ (Poppe 2016) and the mass of the impactors as $m_{\rm imp} = 10^{-8}$ kg. When IDPs enter Saturn's Hill sphere, the planet's gravitational force is responsible for enhancing the flux and velocity of the projectiles (Krivov et al. 2003). Respectively, the mass flux and velocity of IDPs at an orbital radius r are (Colombo, Lautman & Shapiro 1966; Krivov et al. 2003):

$$\frac{F_{\rm imp}}{F_{\rm imp}^{(\infty)}} = \frac{1}{2}\left(\frac{v_{\rm imp}}{v_{\rm imp}^{(\infty)}}\right)^2 + \frac{1}{2}\frac{v_{\rm imp}}{v_{\rm imp}^{(\infty)}}\left[\left(\frac{v_{\rm imp}}{v_{\rm imp}^{(\infty)}}\right)^2 - \left(\frac{R_S}{r}\right)^2\left(1+\frac{2GM_S}{R_S(v_{\rm imp}^{(\infty)})^2}\right)\right]^{1/2}, \tag{9}$$

and

$$\frac{v_{\rm imp}}{v_{\rm imp}^{(\infty)}} = \sqrt{1+\frac{2GM_S}{r\left(v_{\rm imp}^{(\infty)}\right)^2}}. \tag{10}$$

5.1.2 *E ring impactors*

We assume the E ring is composed of sub-micrometric ejecta from Enceladus on to highly eccentric orbits (Nicholson et al. 1996; Kempf et al. 2008; Postberg et al. 2008; Ye et al. 2014a). The average mass of impactors is assumed to be $m_{\rm imp} = 2.3 \times 10^{-15}$ kg (0.65 μm, Spahn et al. 2006) and the impact velocity is given by (Hamilton & Burns 1994; Spahn et al. 2006):

$$v_{\rm imp} = \frac{1}{2}\sqrt{\frac{GM_S}{r}} \tag{11}$$

The flux of impactors on the equator plane is assumed to be $F_{\rm ERP} = m_{\rm imp} v_{\rm imp} N_{\rm ERP}$, where $N_{\rm ERP}$ is the particle number density in the E ring, extracted from the Cosmic Dust Analyser data (Kempf et al. 2008):

$$N_{\rm ERP}(r) = N_0 \exp\left(-\frac{z_0(r)^2}{2\sigma(r)^2}\right)\begin{cases}\left(\frac{r}{3.98\ R_S}\right)^{50} & \text{for } r\le 3.98\ R_S\\ \left(\frac{r}{3.98\ R_S}\right)^{-20} & \text{for } r>3.98\ R_S,\end{cases} \tag{12}$$

with

$$\sigma(r) = 1826\,\mathrm{km} + (r-3.98\ R_S)\begin{cases}-\frac{467\ \mathrm{km}}{0.82\ R_S} & \text{for } r\le 3.98\ R_S\\ \frac{510\ \mathrm{km}}{0.77\ R_S} & \text{for } r>3.98\ R_S,\end{cases} \tag{13}$$

and

$$z_0(r) = \begin{cases}-1220\left(\frac{r-3.98\ R_S}{0.82\ R_S}\right)\ \mathrm{km} & \text{for } r\le 3.98\ R_S\\ 0 & \text{for } r>3.98\ R_S,\end{cases} \tag{14}$$

where N_0 is the maximum particle number density – near Enceladus' radius – set as $N_0 = 1\ \mathrm{m^{-3}}$ (Ye et al. 2014b).

5.1.3 *Mass production rate of Aegaeon, Anthe, Methone, and Pallene*

Following the prescription described in Sections 5.1.1 and 5.1.2 and using equation (7), we estimate the mass production rate of Pallene as

$$M^{+} \sim 7.4\times10^{-4}\,\mathrm{kg\,s^{-1}}. \tag{15}$$

Downloaded from https://academic.oup.com/mnras/article/511/3/4202/6462913 by INIST-CNRS INSU user on 20 April 2023

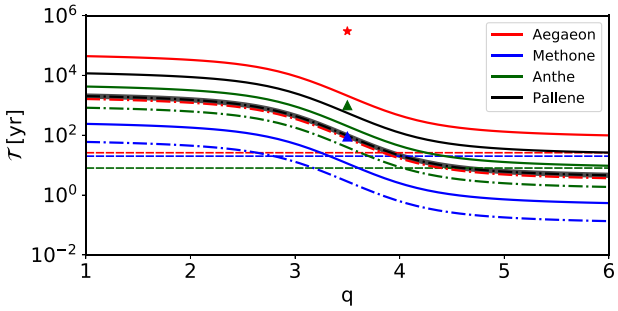


Figure 10. Estimated time $\mathcal{T}$ for Aegaeon, Methone, Anthe, and Pallene to produce the mass of their associated arc/ring as a function of the slope q of the particle radius distribution. The solid and dashed lines correspond to the time calculated following the prescription given in Section 5.1. The solid (dash–dotted) black line corresponds to Pallene's system assuming a non-porous (porous) satellite and the grey area gives the error in the calculation of $\mathcal{T}$ due to the uncertainties in Pallene's bulk density. The coloured red, blue, and green lines correspond to the arcs of Aegaeon, Methone, and Anthe, respectively. The arc lifetime is given by different coloured dashed lines. The red star gives $\mathcal{T}$ obtained for Aegaeon by M18 and the triangles the times obtained for Methone (blue) and Anthe (green) by M20.

In order to determine whether Pallene can maintain the ring, we need to estimate the mass of the structure and compare it with the lifetime of the ejected material, which is obtained by N-body numerical simulations in Section 5.4. If the time $\mathcal{T}$ for Pallene to produce the amount of mass observed in the ring is shorter than the particles' lifetime, then the satellite is an efficient source for the ring and the structure will be in a steady state. On the other hand, if $\mathcal{T}$ is longer than the lifetime of the particles, the ring will disappear unless another source keeps it in a steady-state.

The time for the satellite to produce the observed mass of the ring is (M20)

$$\mathcal{T} = M_{\rm Ring}/M^{+}, \tag{16}$$

if $M_{\rm Ring}$ is the mass of a ring (or arc), as given by (Sfair & Giuliatti Winter 2012):

$$M_{\rm Ring} = A\left(\frac{4}{3}\pi\rho_{\rm ice}\right)\int_{0.1\ \mu{\rm m}}^{100\ \mu{\rm m}} C\pi s^{3-q}{\rm d}s, \tag{17}$$

where s is the physical radius of the particles, C is a constant, and q is the slope of the size distribution of the particles. The surface area is $A = r\Delta\theta\Delta r/2$ (M20), where $\Delta\theta$ is the angular width of the ring/arc in radians and Δr is the radial width. The constant C can be obtained from the observed optical depth τ (Sfair & Giuliatti Winter 2012)

$$\tau = \int_{0.1\ \mu{\rm m}}^{100\ \mu{\rm m}} C\pi s^{2-q}{\rm d}s. \tag{18}$$

The distribution of particles in Pallene's ringlet is not constrained by observational data. However, the data regarding the size distribution of the E ring provide us with a range of possible slopes q for the ringlet, with values ranging from 1.9 to 5 (Horányi, Juhász & Morfill 2008; Kempf et al. 2008; Ye et al. 2014a; Srama et al. 2020). For instance, Horányi et al. (2008) estimated from numerical simulations that the grain density in the E ring follows a power-law distribution with $q = 2.5$, while Kempf et al. (2008) obtained slopes between 4 and 5 for $s > 0.9$ μm from Cassini data. The slopes reported by Ye et al. (2014a) vary between 3 and 4 for $s > 10$ μm. To cover all possible values of q, we assume slopes between 1 and 6.

Fig. 10 shows the time $\mathcal{T}$ for Pallene to produce the ringlet mass (solid black line) for slopes between 1 and 6, assuming a non-porous satellite (equation 7). The figure also shows the time for the moons Aegaeon, Methone, and Anthe to produce the material of their associated arcs (solid coloured lines). Meanwhile, the dash–dotted lines provide the estimated production time $\mathcal{T}$ assuming that the satellites are porous. For Aegaeon, Anthe, and Methone, we assume a bulk density of 500 kg m^{-3}, while for Pallene this value is 250 kg m^{-3}. The filled region surrounding the dashed black line gives the $\mathcal{T}$ calculated using the minimum and maximum bulk densities estimated for Pallene ($\rho_{\rm Pal} = 190$–340 kg m^{-3}). The mass production rate depends only on the cross-section of the satellite, so if we assume a non-porous Pallene, the uncertainties regarding its bulk density do not affect the mass production, since the physical radius of the satellite is constrained by observational data (Hedman et al. 2009).

M18 and M20 estimated $\mathcal{T}$ following a simple prescription assuming production due to IDP impacts of cometary origin (with lower focused fluxes and velocities than the EKB grains), and assumed a single slope, $q = 3.5$. The prescription here presented goes a step further in relation to their model because it incorporates recent data and the production due to ERP impacts. The time $\mathcal{T}$ obtained in M18 for the arc of Aegaeon is shown by the red star in Fig. 10 and the times obtained in M20 for the arcs of Methone and Anthe are the triangles with matching colours. The dashed lines correspond to the lifetime of 10 μm-sized particles, obtained by M18 and M20.

Our times are shorter than those estimated in previous works. M18 obtained that Aegaeon's arc will most likely disappear if it is composed exclusively of micrometre-sized grains. Here, we also obtained that a non-porous Aegaeon cannot replenish the arc material when we disregard other sources in the arcs,[2] since $\mathcal{T}$ is at least an order of magnitude higher than the lifespan of the particles. However, if we mimic the effect of porosity on the yield, the satellite can maintain the arc for $q \gtrsim 4$. Unlike M20, Methone can replenish the arc material for $q > 3.3$ regardless of its porosity. Although the lifetime of the particles in Anthe's arc is shorter than our $\mathcal{T}$ for the non-porous case, the radial width of the arc is unknown [3] and we cannot be sure if the satellite can produce by itself the amount of material necessary to keep the arc in a steady-state or not. Assuming a porous limit, the Anthe arc seems to be in a steady-state for $q \gtrsim 4$.

Table 5 summarizes the initial ring (arc) parameters and the estimated fraction of yield, flux, and mass production between the IDP and ERP populations. We also include the total mass production

Table 5. Radial width (Δr), angular width ($\Delta\theta$), and optical depth (τ) assumed for the systems of Aegaeon, Methone, Anthe, and Pallene (Hedman et al. 2009, 2010, 2020; Sun et al. 2017; Spahn et al. 2019). The table shows the fractions of yield Y, flux F, and mass rate M^{+} between the IDP and ERP, and the total mass rate production in kg s^{-1}.

	Aegaeon	Methone	Anthe	Pallene
Δr [km]	250	1000	1000	2500
$\Delta\theta$ [°]	60	10	20	360
τ	10^{-5}	10^{-6}	10^{-6}	10^{-6}
$Y_{\rm IDP}/Y_{\rm ERP}$	–	447	448	449
$F_{\rm IDP}/F_{\rm ERP}$	–	10	4	10^{-1}
$M^{+}_{\rm IDP}/M^{+}_{\rm ERP}$	–	4×10^{3}	2×10^{3}	50
M^{+}[kg s^{-1}]	2.6×10^{-5}	3.7×10^{-4}	4.2×10^{-5}	7.4×10^{-4}

[2]We do not compute production due to ERPs because Aegaeon is immersed in the G ring.

[3]We assume the same radial width as Methone's arc due to the proximity of the systems and the similar evolution of the particles under the effects of the 14:15 and 10:11 corotation resonance.

Downloaded from https://academic.oup.com/mnras/article/511/3/4202/6462913 by INIST-CNRS INSU user on 20 April 2023

for Aegaeon, Methone, Anthe, and Pallene for the non-porous case. Ejecta production due to IDP impacts is the most efficient for all systems. For the arcs of Aegaeon, Methone, and Anthe, production due to ERPs can be disregarded because the M^+ due to IDP impacts is more than 1000 times higher than for ERPs. The production due to ERPs corresponds to 2 per cent of the total amount produced by Pallene.

5.2 Dynamical model

We study the evolution and fate of Pallene's ringlet by analysing the temporal evolution of two distinct sets of particles: (i) particles initially co-orbital to the satellite (Section 5.3) and (ii) particles ejected from Pallene's surface (Section 5.4). The first set corresponds to a scenario in which the ringlet, and perhaps Pallene, would have formed by a disruption of an ancient satellite, while the second mimics the evolution of the material produced by impacts into the satellite (Section 5.1).

The numerical simulations were performed using MERCURY6 (Chambers 1999) with the Bulirsch–Stoer algorithm. We used 5000 particles with micrometric sizes ranging from 0.1 to 100 μm, and integrated the system until either all particles collide with Mimas, Pallene, or Enceladus or migrate outwards beyond the orbit of Enceladus. We adopted the collision detection treatment between particles and satellites as implemented in MERCURY6 (for details, see Chambers 1999; Liu et al. 2016).

Micrometre-sized particles are affected by non-gravitational forces that decrease their lifetimes. Thus, it is necessary to include these effects in the system. In our simulations, the particles are under the effect of a total force,

$$\vec{\mathrm{F}} = \vec{\mathrm{F}}_{\mathrm{SR}} + \vec{\mathrm{F}}_{\mathrm{PD}} + \vec{\mathrm{F}}_{\mathrm{EM}} + \vec{\mathrm{F}}_{\mathrm{G}}, \tag{19}$$

where $\vec{\mathrm{F}}_{\mathrm{SR}}$ is the solar radiation force, $\vec{\mathrm{F}}_{\mathrm{PD}}$ is the plasma drag force, $\vec{\mathrm{F}}_{\mathrm{EM}}$ is the electromagnetic force, and $\vec{\mathrm{F}}_{\mathrm{G}}$ corresponds to the sum of the gravitational forces of the system: Saturn (including its gravitational coefficients), Mimas, Enceladus, Tethys, Dione, Rhea, Titan, and Pallene.

5.2.1 *Non-gravitational forces*

The solar radiation force ($\vec{\mathrm{F}}_{\mathrm{SR}}$) includes two components (Burns, Lamy & Soter 1979; Mignard 1984): the radiation pressure (RP) caused by collisions of solar radiation on the dust grain,

$$\vec{\mathrm{F}}_{\mathrm{RP}} = \frac{\Phi \pi s^2}{c} Q_{pr} \frac{\vec{r}_{sp}}{r_{sp}}, \tag{20}$$

and the Poynting–Robertson drag (PR), caused by the re-emission of the solar radiation absorbed by the particles,

$$\vec{\mathrm{F}}_{\mathrm{PR}} = -\frac{\Phi \pi s^2}{c} Q_{pr} \left\{ \frac{\vec{V}_P + \vec{V}}{c} + \left[\left(\frac{\vec{V}_P}{c} + \frac{\vec{V}}{c} \right) \cdot \frac{\vec{r}_{sp}}{r_{sp}} \right] \frac{\vec{r}_{sp}}{r_{sp}} \right\}, \tag{21}$$

where c is the speed of light, Φ is the solar flux (Burns et al. 1979), and $\vec{V}$ is the velocity vector of the particle relative to the planet. The solar radiation pressure efficiency Q_{pr} (in equations 20 and 21) depends on the radius of the particle and is computed from Mie theory (Irvine 1965; Mishchenko et al. 1999; Mishchenko, Travis & Lacis 2002) assuming spherical ice grains. The particle is in a circumplanetary orbit $\vec{r}$ ($r = |\vec{r}|$), and the planet in a circular heliocentric orbit. The heliocentric position of Saturn $\vec{r}_{sp}$ ($r_{sp} = |\vec{r}_{sp}|$) and the magnitude of the planet's velocity $\vec{V}_P$ are considered constants. We also assume that Saturn shields particles from solar radiation when the planet eclipses the Sun from the particle's perspective, i.e. the solar radiation force is neglected when the particle is in the planet's shadow, which happens when $\vec{r} \cdot \vec{r}_{sp} < 0$ and $(r^2 - R_{\mathrm{S}}^2) r_{sp} - |\vec{r} \cdot \vec{r}_{sp}|^2 < 0$ (Liu et al. 2016).

The principal source of plasma for Saturn's magnetosphere in the E ring region is the ionization of neutrals provided by the Enceladus plume. The E ring region is dominated by water group ions, i.e. O^+, OH^+, H_2O^+, and H_3O^+, the O^+ ion being the most abundant (Cassidy & Johnson 2010; Tseng et al. 2010; Tseng & Ip 2011; Sittler & Johnson 2015). Direct collision of the plasma with the ring particles is responsible for a drag force ($\vec{\mathrm{F}}_{\mathrm{PD}}$) (Morfill & Gruen 1979; Morfill, Havnes & Goertz 1993; Horányi et al. 2008), given by

$$\vec{\mathrm{F}}_{\mathrm{PD}} = \pi s^2 m_i N_i a^2 (n - \Omega_{\mathrm{S}})^2 \hat{u}_t, \tag{22}$$

where n is the mean motion of the particle, m_i and N_i are the mass and number density of the plasma ions, respectively, and $\hat{u}_t$ is the unit vector in the tangential direction to the osculating orbit of the particle.

Cassini measurements have shown seasonal variations in ion densities ranging from $N_i \sim 40$ cm^{-3} to $N_i \sim 120$ cm^{-3} in Pallene's vicinity (Elrod et al. 2014; Persoon et al. 2015, 2020). For simplicity, we assume the plasma in the Pallene region is only composed of O^+ ions (molecular mass of 16 a.m.u.) with constant number density $N_i = 65.9$ cm^{-3} (Persoon et al. 2015). Moreover, we neglect the indirect Coulomb interaction between charged ring particles and the plasma material, since this effect is at least two orders of magnitude weaker than the direct collisions (Northrop & Birmingham 1982; Grun, Morfill & Mendis 1984; Sun, Schmidt & Spahn 2015).

The ring particles are also influenced by Saturn's magnetosphere due to the charging of the particles by the ambient plasma and electrons photoemission (solar UV). Therefore, the electromagnetic force ($\vec{F}_{\mathrm{EM}}$) (Northrop & Birmingham 1982; Burns et al. 1985) is included in our simulations as

$$\vec{\mathrm{F}}_{\mathrm{EM}} = \frac{4\pi \epsilon_0 s V}{c} \left\{ \left[\vec{V} - \Omega_{\mathrm{S}} (\hat{u}_n \times \vec{r}) \right] \times \vec{B} \right\}, \tag{23}$$

where $\epsilon_0 = 8.8542 \times 10^{-12}$ F m^{-1} is the vacuum permittivity (Chapman & Bartels 1940), V is the electric potential, $\vec{B}$ is the magnetic field vector, and $\hat{u}_n$ is the unit vector perpendicular to the planet's equatorial plane. We adopt an equilibrium potential of $V = -3$ V for the Pallene region, as determined by Hsu et al. (2011) in their investigation of the dynamics of the Saturnian stream particles.

We assumed the Saturnian magnetic field as a composition of an aligned dipole and a quadrupole (Chapman & Bartels 1940; Hamilton 1993):

$$\vec{B} = g_{1.0} R_{\mathrm{S}}^3 \vec{\nabla} \left(\frac{\cos \zeta}{r^2} \right) + \frac{g_{2.0}}{2} R_{\mathrm{S}}^4 \vec{\nabla} \left(\frac{3 \cos^2 \zeta - 1}{r^3} \right), \tag{24}$$

where $g_{1.0} = 0.21$ G is the Saturnian dipole momentum and $g_{2.0} = 0.02$ G, the quadrupole momentum (Hamilton 1993; Belenkaya, Cowley & Alexeev 2006); ζ is the angle between $\hat{u}_n$ and $\vec{r}$.

5.2.2 *Orbital elements of one representative particle*

The non-gravitational forces are responsible for variations in the shape and orientation of the orbits, affecting the temporal evolution of the particles. The mean temporal variations of the osculating orbital elements of a particle with mass m are (Mignard 1984; Hamilton 1993; M20)

$$\dot{a} = -\frac{2na^2\alpha_{\mathrm{r}}}{c} \frac{5 + \cos^2 I}{6} + \frac{2|\vec{F}_{\mathrm{PD}}|}{mn} \sqrt{1 - e^2}, \tag{25}$$

Downloaded from https://academic.oup.com/mnras/article/511/3/4202/6462913 by INIST-CNRS INSU user on 20 April 2023

$$\dot{e} = \alpha_r \sqrt{1-e^2}(\cos\Omega \sin\omega + \sin\Omega \cos\omega \cos I) \quad (26)$$
$$-\frac{3}{2}\frac{e|\vec{F}_{PD}|}{mna}\sqrt{1-e^2} - \frac{q g_{1.0} R_S^3 \Omega_S}{4mcna^3} e\sqrt{1-e^2}\sin^2 I \sin 2\omega,$$

$$\dot{I} = \frac{\alpha_r e}{\sqrt{1-e^2}}\sin\Omega\cos\omega\sin I + \frac{3}{2}\frac{|\vec{F}_{PD}|}{mna}\sqrt{1-e^2}\sin I \quad (27)$$
$$+\frac{q g_{1.0} R_S^3 \Omega_S}{8mcna^3}\frac{e^2}{\sqrt{1-e^2}}\sin 2I \sin 2\omega,$$

$$\dot{\Omega} = -\dot{\Omega}_{obl} + \frac{\alpha_r e}{\sqrt{1-e^2}}\sin\Omega\sin\omega - (2-e)\frac{|\vec{F}_{PD}|}{mna}\cos I\sqrt{1-e^2} \quad (28)$$
$$+\frac{q g_{1.0} R_S^3 \Omega_S}{mcna^3}\frac{1}{\sqrt{1-e^2}}\left[\cos I - \frac{1}{(1-e^2)}\left(\frac{n}{\Omega_S}\right)\right],$$

and

$$\dot{\varpi} = \dot{\varpi}_{obl} + \frac{\alpha_r\sqrt{1-e^2}}{e}(\cos\Omega\cos\omega - \sin\Omega\sin\omega\cos I) \quad (29)$$
$$+(2-e)\frac{|\vec{F}_{PD}|}{mna}\sqrt{1-e^2} + \frac{q g_{1.0} R_S^3 \Omega_S}{mcna^3}\frac{2\cos I}{(1-e^2)^{3/2}}\left(\frac{n}{\Omega_S}\right),$$

where

$$\alpha_r = \frac{3\Phi\pi s^2}{2mcna} Q_{pr}. \quad (30)$$

$\dot{\Omega}_{obl}$ and $\dot{\varpi}_{obl}$ are the temporal variation of longitude of ascending node and argument of pericentre, respectively, due to the non-sphericity of Saturn (see Renner & Sicardy 2006).

Fig. 11 illustrates the variation of geometric orbital elements (a, e, I, Ω and ϖ) of one representative 10 μm particle due to each non-gravitational force and the total force (equation 19). The particle is initially co-orbital to Pallene with $\lambda = \lambda_{Pal} + 180°$, where λ and λ_{Pal} are the mean longitude of the particle and Pallene, respectively. As one can see in the top panel of Fig. 11 (equation 25), the semimajor axis is affected secularly by two distinct drag effects: the Poynting–Robertson component that produces an inward migration, and the plasma drag, which increases the semimajor axis of the particle. We find that the plasma drag is at least one order of magnitude stronger than the Poynting–Robertson component for all particle sizes. While the electromagnetic force only induces short-term variations in the semimajor axis, the net outcome is that grains migrate outward when all the effects are included.

In the eccentricities, we have that the electromagnetic and solar radiation forces produce oscillations with constant period and amplitude for the same particle size (Hamilton 1993; M18; Gaslac Gallardo et al. 2020). As we can see in equation (26), the intensity of these effects depends on the radius of the particles, with $\dot{e} \propto s^{-3}$ for the electromagnetic force and $\dot{e} \propto s^{-1}$ for solar radiation. Thus, the effect of the electromagnetic force dominates over the solar radiation for smaller particles, while for larger sizes the electromagnetic force can be disregarded in relation to the solar radiation.

Plasma drag, on the other hand, produces only short-term variations in the eccentricities (M20). The jumps of this element, seen in Fig. 11, result from the crossing of the particle with resonances with Enceladus, as will be shown in Section 5.3. For Pallene ringlet particles, the electromagnetic force dominates for s ≤ 5 μm, while the solar radiation force is the most important effect on the eccentricity of s > 5 μm particles. We obtain that the non-perturbative forces produce only small variations in the inclination ($I \sim 10^{-3}$ deg) for the time intervals considered by us in this section.

The longitude of ascending node and argument of pericentre are mainly affected by the plasma drag, which is responsible for the precession of the elements in relation to Pallene. Fig. 12 displays

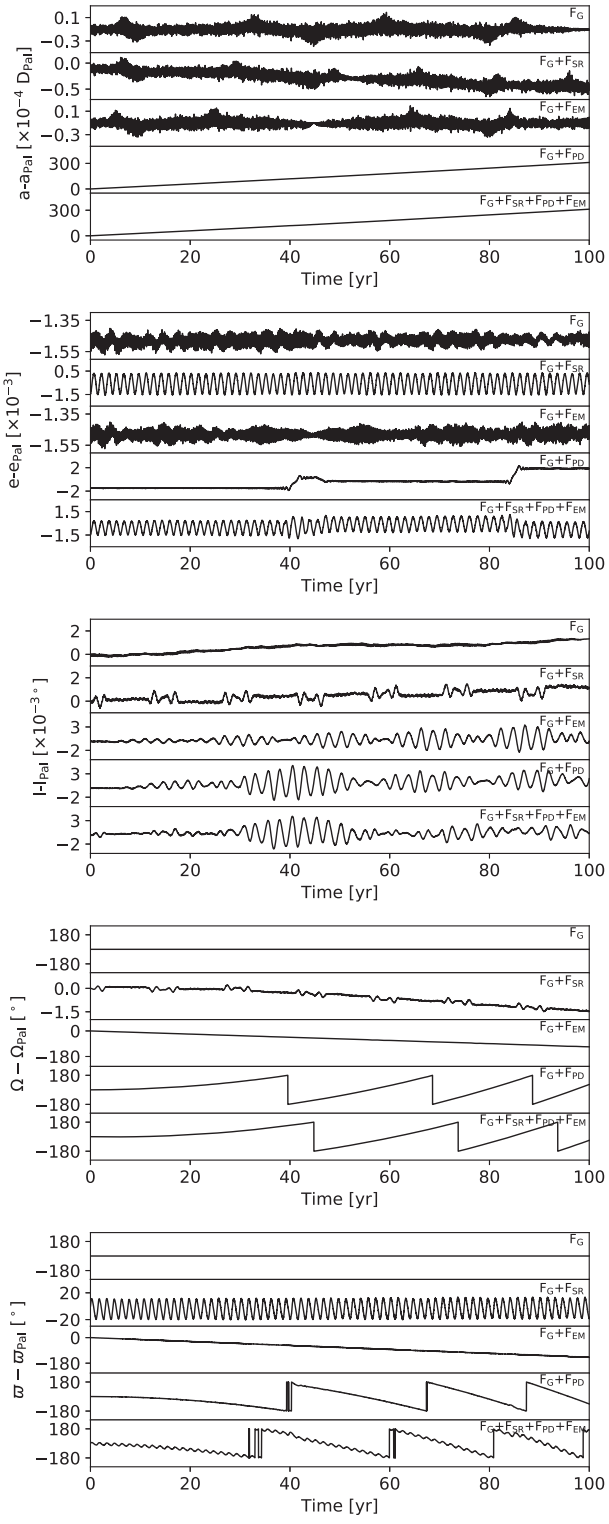


Figure 11. From top to bottom: Geometric semimajor axis, eccentricity, inclination, longitude of ascending node, and argument of pericentre of a 10 μm-sized particle co-orbital to Pallene with displacement in the mean anomaly of 180° in relation to the satellite. The top row of each panel shows the orbital elements when only gravitational effect is included. The following rows display the evolution of the particle when different non-gravitational forces are included (i.e. solar radiation force, electromagnetic force, and plasma drag). Finally, the bottom row of each panel shows the effect of all forces.

Downloaded from https://academic.oup.com/mnras/article/511/3/4202/6462913 by INIST-CNRS INSU user on 20 April 2023

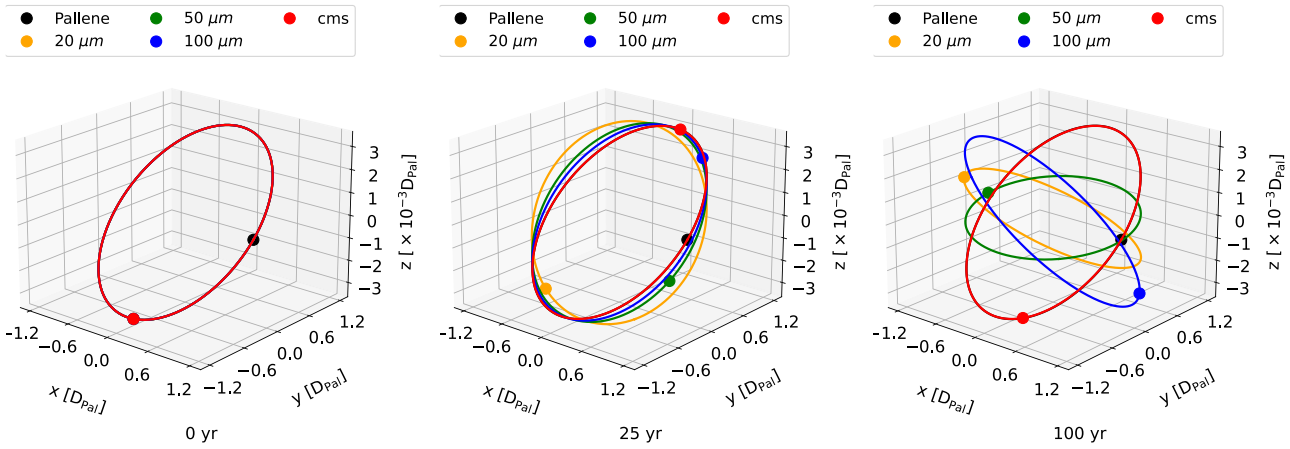


Figure 12. Snapshots of the osculating orbit (solid lines) and spatial position (dots) of Pallene (in black) and of a co-orbital particle with $\lambda = \lambda_P + 90°$. The colour indicates the body, as labelled. We assume the single particle has a radius of either 20, 50, or 100 μm. Displayed in red, we include the case solely with gravitational forces (cms). The orbits are provided in the rotating frame in which Pallene is stationary at $x = 1$ D_{Pal}. An animation of this figure is available for viewing and downloading at tinyurl.com/pallene.

snapshots of the osculating orbit (solid lines) of a representative particle (coloured dots) and Pallene (black dot). We rotate the systems on each snapshot to keep Pallene in the fixed position $x = 1$ D_{Pal}. We show particles with radius of 20, 50, and 100 μm, as well as with radius of centimetres, which corresponds to the case with only gravitational forces.

As we can see in Fig. 12, without non-gravitational forces, the particle remains in the same orbit as Pallene and lacks vertical variation in relation to the satellite's orbital plane. When the non-gravitational forces are included, the orbit precesses, exhibiting vertical excursions in relation to Pallene's orbital plane. This phenomenon could be responsible for the observed vertical width of $\sim 10^2$ km of the ring (Hedman et al. 2009; Spahn et al. 2019) indicating that the ringlet may evolve into a torus, as observed in the gossamer rings of Jupiter (Burns et al. 1999). The formation of the torus occurs when the precession of the pericentre acts long enough to completely randomize the orientation of the particles' orbits. These results will be discussed in detail in Section 5.3.

The osculating semimajor axis and eccentricity of a representative particle under the effects of the non-gravitational forces are presented in Fig. 13. The lines correspond to numerical simulations where the physical radius of the single particle is modified (0.1, 0.2, 0.5, 1, 2, 5, 10, 20, 50, and 100 μm). The solid and dotted horizontal lines indicate the orbits of Pallene and Enceladus, respectively. In this work, we consider a particle to be removed from the ringlet if it collides with a satellite or migrates outside the generous limit of a_{Pal} + 1100 km (∼ 1.05 D_{Pal}). The latter can be seen in the figure by the horizontal dot–dashed line.

Particles with s ≤ 2 μm migrate beyond the orbit of Enceladus (horizontal dotted line) in less than 100 yr and reach $e > 10^{-2}$. In the case shown in Fig. 13, the particles of 0.1 and 1 μm are ejected from the Saturnian system ($e > 1$), while the particles of 0.2 and 0.5 μm collide with a satellite outside the orbit of Enceladus. The 2 μm-sized particle collides with Enceladus in about 80 yr.

The effects of the non-gravitational forces are weaker for larger grains and particles with $s > 5$ μm remain with eccentricities of the order of 10^{-3}. These particles migrate outwards but still are considered ringlet particles according to our definition. These results roughly demonstrate that the permanence of the particles in the ring is strongly affected by non-gravitational forces and only particles with

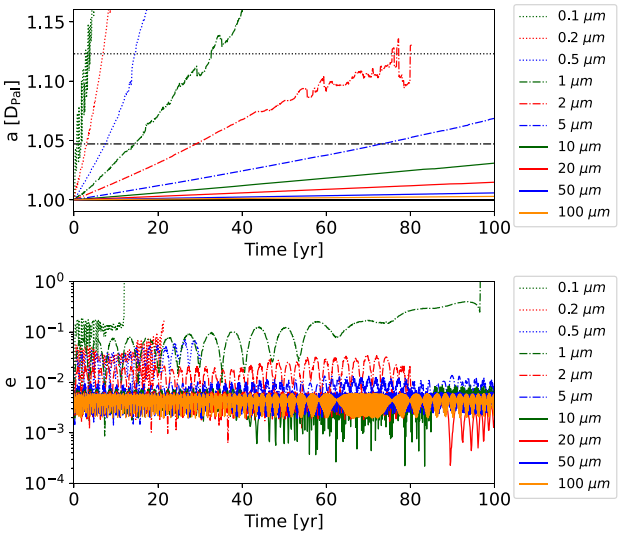


Figure 13. Osculating semimajor axis and eccentricity of representative particles co-orbiting Pallene. The particles have a size of 0.1, 0.2, 0.5, 1, 2, 5, 10, 20, 50, and 100 μm (coloured lines). The horizontal dotted line indicates Enceladus's semimajor axis, while the horizontal dot–dashed line is the maximum semimajor axis of the particle to be considered as a ringlet particle. The particles are under the effects of the solar radiation force, plasma drag, and electromagnetic force.

a radius of tens of micrometres or greater should have significantly long lifetimes in the ringlet (several hundreds of years). In the next sections, we perform full *N*-body simulations of the ring particles evolution.

5.3 Particles co-orbital to Pallene

In this section, we analyse Pallene's ringlet as formed by a set of 5000 particles co-orbital to the satellite. We assume particles with the same orbital elements as Pallene, except for the mean anomaly that was randomly selected from a uniform distribution between 0° and 360°. The ring composed of co-orbital particles corresponds, e.g.

Downloaded from https://academic.oup.com/mnras/article/511/3/4202/6462913 by INIST-CNRS INSU user on 20 April 2023

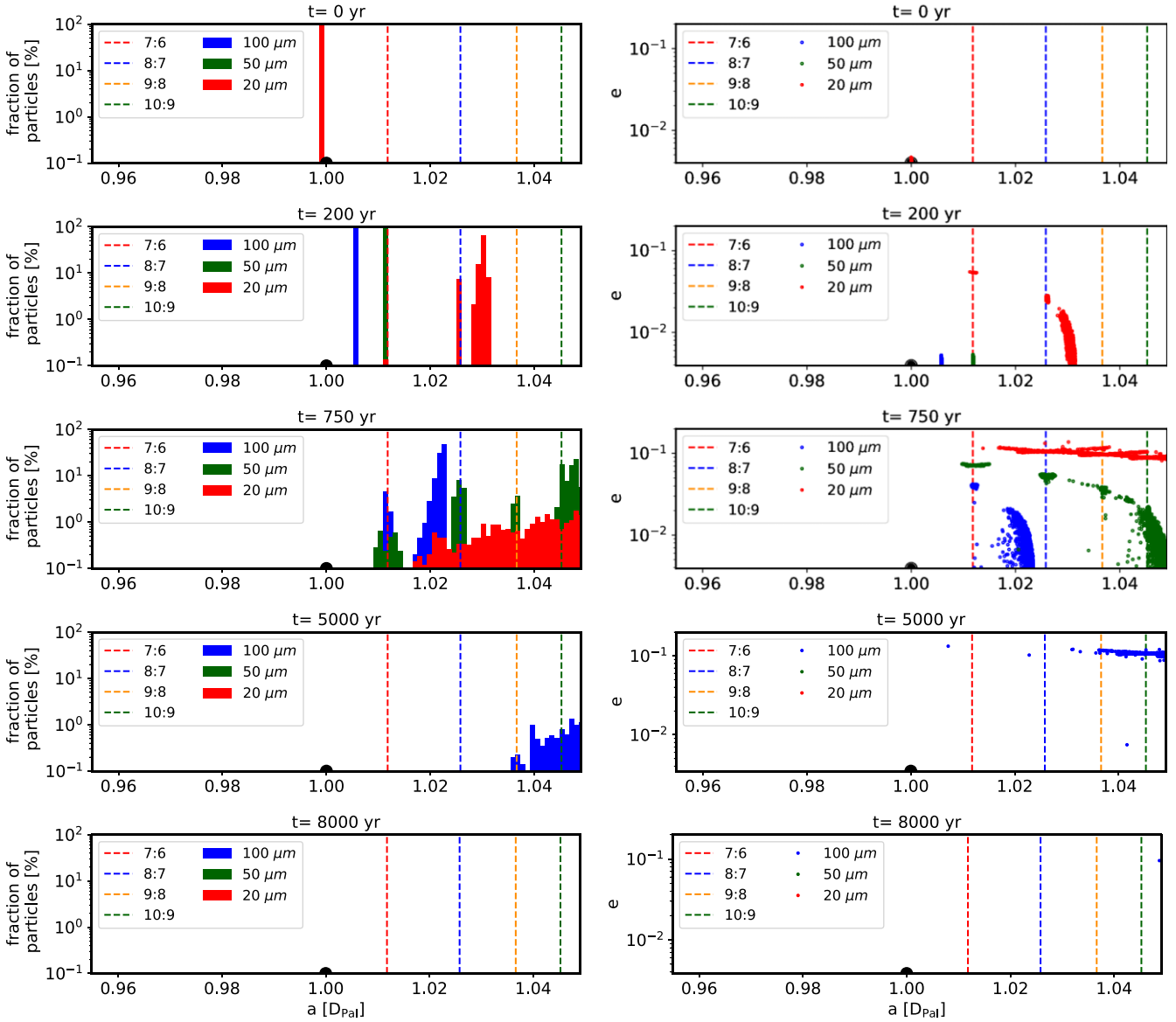


Figure 14. Snapshots showing the percentage of particles as a function of the geometric semimajor axis (at left) and the geometric eccentricity versus geometric semimajor axis (at right). From top to bottom, we show the data for 0, 200, 750, 5000, and 8000 yr. The 20, 50, and 100 μm-sized particles are shown in different colours, as indicated. Pallene is represented by a black filled circle. The locations of MMRs with Enceladus are indicated by dashed vertical lines. Similarly to Fig. 12, an animation of this figure is available for viewing and downloading at tinyurl.com/pallene.

to a scenario where the structure could be formed by the disruption of a proto-Pallene. In this scenario, the ring would also be composed of centimetre-sized or even larger particles. Nevertheless, we do not perform simulations for this size range since the effects of non-gravitational forces can be neglected. The orbital evolution of the centimetre-sized particles would correspond to the analysis in Section 3.2 which demonstrated that most of the particles initially located inside the Pallene collision region would eventually collide with the satellite, reducing the survival rate of co-orbital particles.

As a general outcome, particles with $s \leq 10$ μm present a dynamical evolution similar to those shown in Fig. 11. The particles migrate towards Enceladus and show an increase in eccentricity. However, we obtain a more complex dynamical evolution for particles with $s \geq 20$ μm caused by capture in resonances with Enceladus. Roughly speaking, a migrating particle is captured at a given resonance with a satellite if the migration time-scale is shorter than the libration period of the resonance (Batygin 2015). In our case, this condition is achieved for the largest particles (20, 50, and 100 μm) which are captured, even for a short period of time, in the 7:6, 8:7, 9:8, and 10:9 *e*-type MMRs with Enceladus.

Fig. 14 shows the evolution of the fraction of particles with $s >$ 20 μm (left column), as well as their geometric eccentricity (right column), as a function of the geometric semimajor axis. Initially, all particles have the same semimajor axis and eccentricity as Pallene (black dot). As the particles migrate outward, they cross resonances with Enceladus, increasing their eccentricities. After 200 yr, a fraction of 20 μm-sized particles is trapped in the 7:6 and 8:7 MMRs, while most of the set is located between the 8:7 and 9:8 MMRs. Particles in the 7:6 MMR are confined for a longer period of time, reaching the highest eccentricity values (≈0.05). The

Downloaded from https://academic.oup.com/mnras/article/511/3/4202/6462913 by INIST-CNRS INSU user on 20 April 2023

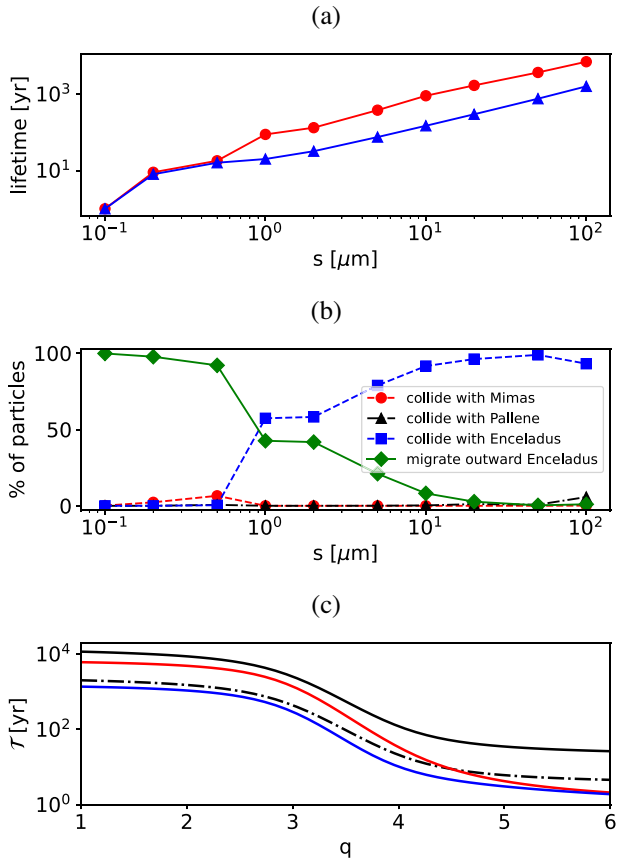


Figure 15. (a) The half-life (in blue) and the lifetime (in red) of the ring as a function of the physical radius of the co-orbital particles. (b) The fraction of the particles that collides with the satellites Mimas (in red), Pallene (in black), and Enceladus (in blue), and the fraction of particles that migrates out of the orbit of Enceladus (in green). (c) The time $\mathcal{T}$ for the satellite to produce the mass of the ring, assuming a non-porous (black solid line) and a porous (black dot–dashed line) Pallene. The red and blue lines give the ring's lifetime and half-life, respectively, as a function of the slope q.

20 μm-sized particles that are not in MMRs at 200 yr had their eccentricity increased during the passage through the two innermost resonances, reaching values ∼0.01. Particles with radius of 50 and 100 μm have not yet crossed any resonances and remain with the same initial eccentricity.

At 750 yr, the 100 μm-sized particles have crossed the 7:6 MMR, and the 50 μm-sized particles have crossed all four resonances. Most of the 20 μm-sized particles migrated outside the limit of ≈1.05 D_{Pal}, leaving only the particles confined in MMRs. A similar result is seen for 5000 yr, when only 100 μm-sized particles in MMRs remain in the ring, indicating that capture in resonances increases their longevity. Therefore, the vicinity of MMRs would correspond to brighter regions of the ring, as will be shown later. Finally, after 8000 yr, the ring is completely depleted of micrometre-sized particles.

Fig. 15(a) shows two different time-scales as a function of particle radius: in blue, the time required for 50 per cent of particles to collide with a satellite or migrate outside the limit of ∼1.05 D_{Pal} – hereafter referred to as the ring's half-lifetime – and in red the time required for all particles to be lost – referred as the ring's lifetime. The ring is completely depleted of sub-micrometric particles in less than a decade, while particles of radius of 1–10 μm have lifetimes of the order of 10^2 yr. Particles that last longer are those with $s \geq 20$ μm, with lifetimes of ∼10^3 yr – same order of the time $\mathcal{T}$ for Pallene to produce the mass of the ring (see Fig. 10).

Particle sinks are shown in Fig. 15(b). Due to the intense migration caused by the plasma drag, almost all the sub-micrometric particles migrate beyond the orbit of Enceladus and collide with an external satellite or are ejected from the system. By increasing the radius of the particles, the slower rate of migration increases the period that the particles interact gravitationally with Enceladus in the vicinity of the satellite. Consequently, the number of collisions with Enceladus increases, as seen in Fig. 15(b). Also due to migration, the number of particles that collide with Pallene is less than 5 per cent for all sizes; this rules out Pallene as an efficient secondary source of material, produced by subsequent impact with these particles.

Fig. 15(c) shows in black lines the same curves shown in Fig. 10: the solid line is the time for Pallene to produce the ring mass in the non-porous case, while the dot–dashed line is the same for the porous case. The red and blue lines indicate the ring's lifetime and half-lifetime, respectively, obtained by a time-weighted average:

$$\bar{T} = \frac{\sum_s m_s \left(\frac{s\ (\mu\mathrm{m})}{100\ \mu\mathrm{m}}\right)^{-q} T_s}{\sum_s m_s \left(\frac{s\ (\mu\mathrm{m})}{100\ \mu\mathrm{m}}\right)^{-q}}, \tag{31}$$

where m_s is the mass of a particle with radius s and T_s is the (half)-lifetime of the particles.

Focusing on the red curve in Fig. 15(c), we verify that the ring would not be in a steady state, assuming ejection by Pallene as the only source of material. However, given the uncertainties in the yield calculation and the proximity of the values between the black and red solid curves, towards the lower values of q, we can conclude that Pallene might be able to maintain its ring if the particle distribution is given by q $\lesssim$ 3. Lower slope values mean that the ring has higher concentrations of larger particles, which seems to be the case of the ringlet of Pallene – given that larger particles can be captured in MMRs with Enceladus, while smaller ones have lifetimes of only a few years. If the particle distribution in the ring is given by slopes q $\gtrsim$ 4, Pallene by itself certainly cannot maintain the ring, since the lifetime is lower than $\mathcal{T}$ even for the porous limit.

Fig. 16 shows animations of the co-orbital particle profiles in the planes θ-r (top panels) and r-z (bottom panels). The colour of each pixel gives the normalized optical depth of that pixel, assuming a particle distribution with slope $q = 2.5$. The particles are initially distributed along the orbit of Pallene. In 10 yr, we can identify ring-like structures in the r-z plane, produced by the precession of the longitude of pericentre (Fig. 12), where each structure is composed of particles with different radii. After 100 yr, the ring shows an asymmetrical profile, with the brightest part close to Pallene's orbit, and structures with lower brightness outside the satellite's orbit. We do not see any bright regions inside the orbit of Pallene, since outward migration is dominant for all particles.

At 400 yr, the torus structure is completely formed, and the ring has an asymmetric structure. The brightest part of the ring is in the region of the 7:6 MMR with Enceladus, but we see dimmer structures inside and outside this location, as an effect of the increased eccentricity of resonant particles. After 1000 yr, the complete structure of the ring has moved outward and the brightest region is located in the 8:7 MMR. After 4000 yr, the structure has moved further away and only a few particles have remained in the ring region.

Downloaded from https://academic.oup.com/mnras/article/511/3/4202/6462913 by INIST-CNRS INSU user on 20 April 2023

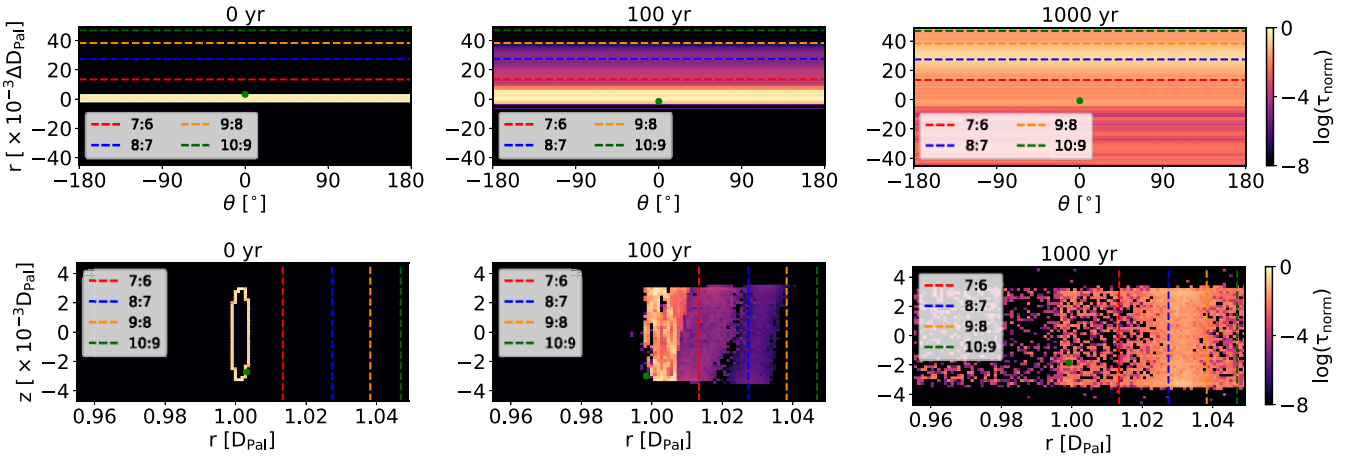


Figure 16. Animations showing the normalized optical depth $\tau_{\rm norm}$ in the θ-r (top panels) and r-z (bottom panels) planes in the rotating frame for co-orbital particles. The green dot gives Pallene's position and the dashed lines indicate the MMRs with Enceladus. The upper limit of the radius in the panels corresponds to the limit 1.05 $D_{\rm Pal}$. An animation of this figure is available for viewing and downloading at tinyurl.com/pallene.

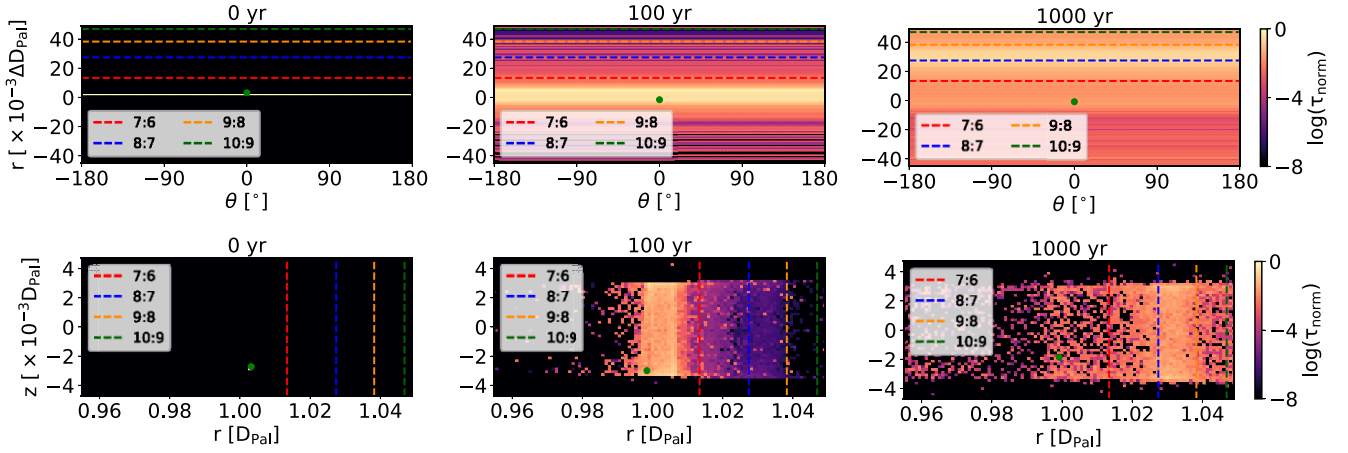


Figure 17. Normalized optical depth $\tau_{\rm norm}$ for the ejected particles. Similarly to Fig. 16, we present a cut in the θ-r and r-z planes in the rotating frame. The green dot gives Pallene's position and the vertical dashed lines are MMRs with Enceladus. An animation of this figure is available for viewing and downloading at tinyurl.com/pallene.

5.4 Particles ejected from Pallene

In the numerical simulations presented in this section, 5000 particles were randomly and uniformly distributed in a spherical shell within the Hill radius of Pallene. Particles are ejected radially with random velocities that follow the normalized distribution (Hartmann 1985; Krivov et al. 2003; Sun et al. 2017):

$$f_v = \frac{1}{v_0}\left(\frac{v}{v_0}\right)^{-2}\Theta[v - v_0], \tag{32}$$

where $\Theta(x)$ denotes the Heaviside function. The minimum ejecta speed, v_0, is obtained from the transcendental equation (Krüger, Krivov & Grün 2000)

$$\frac{K_e}{K_i} = Y\left(\frac{v_0}{v_{\rm imp}}\right)^2\left[\left(\frac{v_0}{v_{\rm max}}\right)^{-1} - 1\right], \tag{33}$$

where $v_{\rm max}$ is the maximum ejecta speed and K_e/K_i is the ratio between the kinetic energy partitioned to the ejecta and the impactor's kinetic energy, assumed as $K_e/K_i = 0.1$ (Sun et al. 2017).

Fig. 17 is similar to Fig. 16 but for the ejected particles. The temporal evolution of the ejected particles is similar to the co-orbital particles scenario. The same is true for the ring profiles, with greater distinctions only in the first years of the simulation, due to the different initial conditions. Fig. 18 shows the half-lifetime and lifetime of the ring (top panel), the particle sinks (middle panel), the times required for Pallene to produce the ring material, as well as the lifetimes as a function of the slope of the size distribution (bottom panel). Our results are similar to those discussed in Section 5.3. In both scenarios, Pallene could produce the material to keep the ring in a steady state if the distribution of the particles in the ring is given by $q \lesssim 3$.

5.5 Comments on ring sources

Similar to M18 and M20, we only computed the production due to external projectile impacts with the immersed moon. Therefore, we are analysing whether the satellite can produce the amount of material needed to keep the systems in steady state, not whether they are in steady state. In fact, the most likely case is that all the mentioned dusty arcs/rings are in a quasi-steady state, demonstrating that more sophisticated models are needed to understand their stability.

As we pointed out in this section, satellite porosity can be a factor influencing material production; however, the systems also have other

Downloaded from https://academic.oup.com/mnras/article/511/3/4202/6462913 by INIST-CNRS INSU user on 20 April 2023

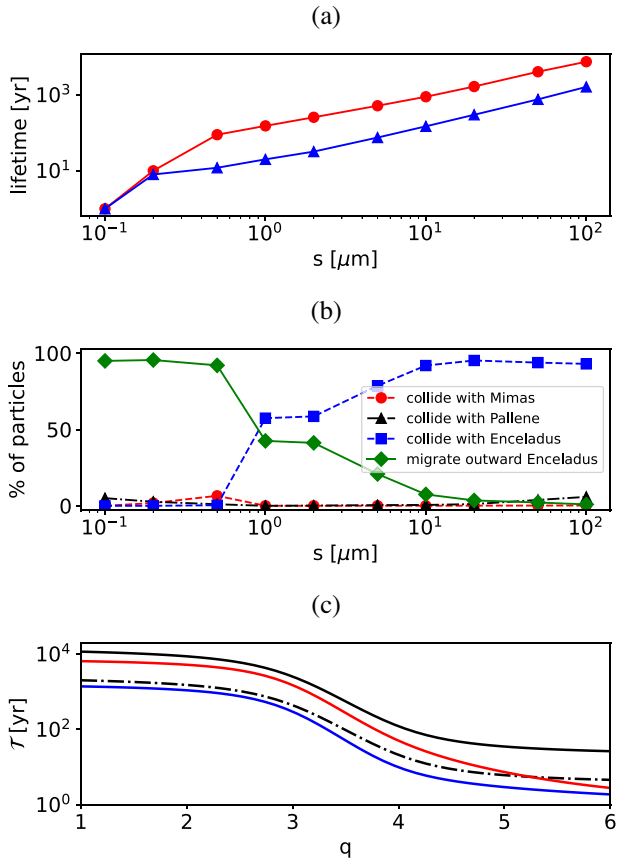


Figure 18. (a) The solid lines in blue and red show the time for 50 per cent and 100 per cent of the ejected particles to be removed from Pallene ring, respectively. (b) The coloured lines show the fraction of particles that collide with Mimas (in red), Pallene (in black), and Enceladus (in blue), and the fraction that migrates outside the orbit of Enceladus (in green). (c) The time for Pallene to produce the ring material is given by the black lines, in the non-porous (solid) and porous (dot–dashed) cases, while the ring lifetime and half-life are given by the red and blue lines, respectively.

sources. For example, ring particles are also impacted by external projectiles and therefore also produce material. However, following the prescription given in Dikarev et al. (2005), we obtained that such source is at least three orders of magnitude less efficient than the satellite for the systems analysed here.

The mentioned arcs/rings have the similarity of having a population of larger particles (∼cm-m, Hedman et al. 2009, 2010; Spahn et al. 2019), which lead us to speculate whether the mutual collision of these objects or their impacts with the moon would be the main source of these systems (Colwell & Esposito 1990a, b). Just as a proof of concept, we will assume that in the Pallene ring is immersed a family of moonlets with radii ranging from 1 to 100 m, following a size distribution $N \sim s^{-3.5}$ and total optical depth $\tau_{\rm mlets} = 10^{-8}$. Production due to impacts between the moonlets can be roughly estimated as (Sun et al. 2015)

$$\dot{M}_{\rm mlets} = 3\tau_{\rm mlets} N M_{\rm col}, \tag{34}$$

where $M_{\rm col}$ is the amount of dust released per collision, assumed as $0.12 M_{\rm mlet}$ (Canup & Esposito 1995), and $M_{\rm mlet}$ is the total mass of the moonlet population.

As a result, we get $\dot{M}_{\rm mlets} \sim 10^{-2}$ kg s^{-1} corresponding to a value more than one order of magnitude higher than the production due to the non-porous Pallene. This shows that impacts between larger particles are an appealing possibility to keep the arcs/rings in steady state. However, production due to impacts between centimetric-metric bodies is a very intricate problem, and is beyond the scope of this work.

6 SUMMARY AND CONCLUSIONS

In this work, we performed an exhaustive numerical exploration of the evolution of the small Saturnian moon Pallene, as well as of the diffuse dusty ring sharing its orbit. We used both short- and long-term numerical simulations, spanning a wide range of time-scales to cover in detail the evolution of Pallene and its ring.

Using the frequency map analysis technique, we produced a diffusion map to characterize the current dynamical state of a wide region of phase-space surrounding Pallene. We identified all the MMRs of relevance in the region, among Pallene and any of the six major moons considered in this study, up to fourth order. We used a simple tidal evolution calculation for Mimas, Pallene, and Enceladus in order to set the context for our longer term simulations. We made note that the most recent resonance Pallene may have escaped from is the 4:5 resonance with Mimas. Pallene's current eccentricity or inclination could be signs of this or another past resonance crossing.

From the short- and long-term N-body simulations, we analysed all the direct and indirect arguments of the disturbing function identified in the diffusion map in the vicinity of Pallene. These arguments included zeroth-order arguments, with degrees $j \leq 15$, and first- to fourth-order arguments with degrees $j \leq 30$. In brief, we found that some arguments displayed interesting behaviour by temporally librating at various time-scales. In particular, the direct argument $\phi_{\rm tP} = 8\lambda' - 5\lambda - \varpi' - 2\varpi$ of Pallene with Tethys that librates for ∼10 kyr and the zeroth-order argument $\Phi = \varpi' - \varpi + \Omega' - \Omega$ of Pallene with Tethys, Dione and Titan, which coincides with the angle combination suggested for Pallene with Mimas by Callegari & Yokoyama (2010). The recurrence of this zeroth-order combination suggests a possible secular alignment of the lines of apsides and nodes among Pallene, Dione, Rhea, and Titan in time-scales ∼800 yr.

Furthermore, after a thorough search of possible (two-body) resonant arguments for Pallene, we conclude that the small moon is not currently in resonance with either Mimas, Enceladus, Tethys, Dione, Rhea, or Titan. It is unlikely that Pallene would be in a higher order MMR, i.e. ≥fifth order, with any of these satellites, due to their small eccentricity/inclination, and the corresponding e-I coefficients of the disturbing function. Nevertheless, the lack of two-body MMRs for Pallene does not exclude the hypothesis that Pallene might be part of a three-body resonance. Moreover, under the present considerations and without accounting for Saturn's tidal forces in the numerical simulations, we cannot dismiss either the past escape of Pallene from a resonance or its future trapping, particularly at times longer than 5 Myr.

We analysed the dynamical evolution of the Pallene ring assuming a scenario where particles are ejected from the satellite's surface, as well as a scenario where the material is originally co-orbital to Pallene. We found that non-gravitational forces dynamically dominate the system and the material experiences a similar dynamical evolution in both scenarios.

The outward migration due to plasma drag causes the loss of particles with radius of a few micrometres in just tens of years, while larger particles (≳10 μm) can survive for a few hundred years in the ring. Spahn et al. (2019) measured the radial mean position of the ring to be more than 1000 km beyond the satellite's orbit; this is likely caused by plasma drag. Our ring profiles clearly show the formation of particle clusters beyond Pallene's orbit. Furthermore,

Downloaded from https://academic.oup.com/mnras/article/511/3/4202/6462913 by INIST-CNRS INSU user on 20 April 2023

the profiles show that the ring evolves into structures that are radially asymmetrical in relation to the satellite's orbit.

The precession of the longitude of pericentre due to non-gravitational forces produces vertical excursions of the particles in relation to Pallene's orbital plane. This could be the mechanism responsible for vertical excursions discussed in Hedman et al. (2009).

Cassini data indicate a concentration of larger particles around Pallene's orbit, which is in line with the significantly longer lifetime of the larger particles that we found. In fact, when calculating the mass production rate due to IDPs and ERPs, we find that Pallene can keep the ring in a steady-state only if it is predominantly composed of larger micrometre-sized particles ($q \lesssim 3$).

If we assume Pallene as the only source of material for the rings, we conclude that the ring would spread for $q \lesssim 4$. This corresponds to the slope range given by Kempf et al. (2008) and Ye et al. (2014a) for the E ring, in which Pallene is immersed. In this scenario, our profiles show that the ring will evolve into a toroidal structure similar to the gossamer rings of Jupiter, and then it will continuously spread out, both radially and vertically, until it finally disappears. From our numerical results, we cannot constrain whether the ring originated from the material ejected from the satellite or from the disruption of an ancient proto-Pallene.

We must point out that our dynamical model is not complete; if the ring has a high concentration of larger particles, additional effects such as collisions between the particles, self-gravity, and local viscosity may be significant to the system. However, even in this case, plasma drag may dominate, and our main results would still hold valid.

ACKNOWLEDGEMENTS

We thank the anonymous referee for a detailed and careful report that helped to greatly improve the quality of this paper. G. Madeira thanks FAPESP for financial support via grant 2018/23568-6. J. A'Hearn thanks M. Hedman, M. Tiscareno, and M. Showalter for useful discussions; and also thanks NASA for partial support through the *Cassini* Data Analysis and Participating Scientist Program grant NNX15AQ67G. S. M. Giuliatti Winter thanks FAPESP (2016/24561-0), CNPq (313043/2020-5), and CAPES for the financial support.

DATA AVAILABILITY

The data underlying this article will be shared on reasonable request to the corresponding author.

REFERENCES

Allan R. R., 1969, AJ, 74, 497
Altobelli N., Kempf S., Postberg F., Fischer C., Albin T., Srama R., 2018, in European Planetary Science Congress. Berlin, Germany, p. EPSC2018–199
Archinal B. A. et al., 2011, Celest. Mech. Dyn. Astron., 109, 101
Batygin K., 2015, MNRAS, 451, 2589
Belenkaya E. S., Cowley S. W. H., Alexeev I. I., 2006, Ann. Geophys., 24, 1649
Boué G., Fabrycky D. C., 2014, ApJ, 789, 111
Burns J. A., Lamy P. L., Soter S., 1979, Icarus, 40, 1
Burns J. A., Schaffer L. E., Greenberg R. J., Showalter M. R., 1985, Nature, 316, 115
Burns J. A., Showalter M. R., Hamilton D. P., Nicholson P. D., de Pater I., Ockert-Bell M. E., Thomas P. C., 1999, Science, 284, 1146
Callegari N., Yokoyama T., 2010, in Fernandez J. A., Lazzaro D., Prialnik D., Schulz R., eds, Proc. IAU Symp. 263, Icy Bodies of the Solar System. Kluwer, Dordrecht, p. 161
Callegari N., Yokoyama T., 2020, Icarus, 348, 113820
Callegari N., Rodríguez A., Ceccatto D. T., 2021, Celest. Mech. Dyn. Astron., 133, 49
Canup R. M., Esposito L. W., 1995, Icarus, 113, 331
Cassidy T. A., Johnson R. E., 2010, Icarus, 209, 696
Chambers J. E., 1999, MNRAS, 304, 793
Chapman S., Bartels J., 1940, Geomagnetism. Vol. I. Geomagnetic and Related Phenomana. Vol. II. Analysis and Physical Interpretation of the Phenomena. Oxford University Press, Oxford, England
Colombo G., Lautman D. A., Shapiro I. I., 1966, J. Geophys. Res., 71, 5705
Colwell J. E., Esposito L. W., 1990a, Geophys. Res. Lett., 17, 1741
Colwell J. E., Esposito L. W., 1990b, Icarus, 86, 530
Cooper N. J., Murray C. D., Evans M. W., Beurle K., Jacobson R. A., Porco C. C., 2008, Icarus, 195, 765
Correia A. C. M., Udry S., Mayor M., Laskar J., Naef D., Pepe F., Queloz D., Santos N. C., 2005, A&A, 440, 751
Ćuk M., Dones L., Nesvorný D., 2016, ApJ, 820, 97
Dikarev V., Grün E., Baggaley J., Galligan D., Landgraf M., Jehn R., 2005, Adv. Space Res., 35, 1282
Divine N., 1993, J. Geophys. Res., 98, 17029
El Moutamid M., Sicardy B., Renner S., 2014, Celest. Mech. Dyn. Astron., 118, 235
El Moutamid M., Sicardy B., Renner S., 2017, MNRAS, 469, 2380
Elrod M. K., Tseng W. L., Woodson A. K., Johnson R. E., 2014, Icarus, 242, 130
Fuller J., Luan J., Quataert E., 2016, MNRAS, 458, 3867
Gaslac Gallardo D. M., Giuliatti Winter S. M., Madeira G., Muñoz-Gutiérrez M. A., 2020, Ap&SS, 365, 5
Giuliatti Winter S., Madeira G., Sfair R., 2020, MNRAS, 496, 590
Granados Contreras A. P., Boley A. C., 2018, AJ, 155, 139
Greenberg R., 1973, MNRAS, 165, 305
Greenberg R., 1975, MNRAS, 170, 295
Grun E., Morfill G. E., Mendis D. A., 1984, in Greenberg R., Brahic A., eds, IAU Colloq. 75: Planetary Rings. University of Arizona Press, Arizona, USA, p. 275
Grun E., Zook H. A., Fechtig H., Giese R. H., 1985, Icarus, 62, 244
Hamilton D. P., 1993, Icarus, 101, 244
Hamilton D. P., Burns J. A., 1994, Science, 264, 550
Hartmann W. K., 1985, Icarus, 63, 69
Hedman M. M., Murray C. D., Cooper N. J., Tiscareno M. S., Beurle K., Evans M. W., Burns J. A., 2009, Icarus, 199, 378
Hedman M. M., Cooper N. J., Murray C. D., Beurle K., Evans M. W., Tiscareno M. S., Burns J. A., 2010, Icarus, 207, 433
Hedman M. M., Helfenstein P., Chancia R. O., Thomas P., Roussos E., Paranicas C., Verbiscer A. J., 2020, AJ, 159, 129
Helled R., Galanti E., Kaspi Y., 2015, Nature, 520, 202
Hesselbrock A. J., Minton D. A., 2019, AJ, 157, 30
Horányi M., Juhász A., Morfill G. E., 2008, Geophys. Res. Lett., 35, L04203
Hsu H. W., Postberg F., Kempf S., Trieloff M., Burton M., Roy M., Moragas-Klostermeyer G., Srama R., 2011, J. Geophys. Res., 116, A09215
Iess L. et al., 2019, Science, 364, aat2965
Irvine W. M., 1965, J. Opt. Soc. Am., 55, 16
Jacobson R. A. et al., 2006, AJ, 132, 2520
Jacobson R. A., Spitale J., Porco C. C., Beurle K., Cooper N. J., Evans M. W., Murray C. D., 2008, AJ, 135, 261
Kaib N. A., Raymond S. N., Duncan M. J., 2011, ApJ, 742, L24
Kempf S. et al., 2008, Icarus, 193, 420
Kempf S., Beckmann U., Schmidt J., 2010, Icarus, 206, 446
Kliore A. J., Patel I. R., Lindal G. F., Sweetnam D. N., Hotz H. B., Waite J. H., McDonough T., 1980, J. Geophys. Res., 85, 5857
Koschny D., Grün E., 2001, Icarus, 154, 391
Krivov A. V., Sremčević M., Spahn F., Dikarev V. V., Kholshevnikov K. V., 2003, Planet. Space Sci., 51, 251
Krüger H., Krivov A. V., Grün E., 2000, Planet. Space Sci., 48, 1457
Lainey V. et al., 2012, ApJ, 752, 14

Downloaded from https://academic.oup.com/mnras/article/511/3/4202/6462913 by INIST-CNRS INSU user on 20 April 2023

Lainey V. et al., 2017, Icarus, 281, 286
Lainey V. et al., 2020, Nat. Astron., Springer Nature, London, UK
Landgraf M., Liou J. C., Zook H. A., Grün E., 2002, AJ, 123, 2857
Laskar J., 1990, Icarus, 88, 266
Laskar J., 1993, Physica D Nonlinear Phenom., 67, 257
Laskar J., Froeschlé C., Celletti A., 1992, Physica D Nonlinear Phenom., 56, 253
Liu X., Sachse M., Spahn F., Schmidt J., 2016, J. Geophys. Res., 121, 1141
Madeira G., Giuliatti Winter S. M., 2020, Eur. Phys. J. Spec. Top., 229, 1527 (M20)
Madeira G., Sfair R., Mourão D. C., Giuliatti Winter S. M., 2018, MNRAS, 475, 5474 (M18)
Meyer J., Wisdom J., 2008, Icarus, 193, 213
Mignard F., 1984, in Greenberg R., Brahic A., eds, IAU Colloq. 75: Planetary Rings. University of Arizona Press, Tucson, Arizona, USA, p. 333
Mishchenko M. I., Dlugach Z. M., Yanovitskij E. G., Zakharova N. T., 1999, J. Quant. Spectrosc. Radiat. Transfer, 63, 409
Mishchenko M. I., Travis L. D., Lacis A. A., 2002, Scattering, Absorption, and Emission of Light by Small Particles. Cambridge University Press, Cambridge, UK
Morfill G. E., Gruen E., 1979, Planet. Space Sci., 27, 1269
Morfill G. E., Havnes O., Goertz C. K., 1993, J. Geophys. Res., 98, 11285
Muñoz-Gutiérrez M. A., Giuliatti Winter S., 2017, MNRAS, 470, 3750
Murray C. D., Dermott S. F., 1999, Solar System Dynamics. Cambridge University Press, Cambridge, UK
Nesvorný D., Jenniskens P., Levison H. F., Bottke W. F., Vokrouhlický D., Gounelle M., 2010, ApJ, 713, 816
Neveu M., Rhoden A. R., 2019, Nat. Astron., 3, 543
Nicholson P. D. et al., 1996, Science, 272, 509
Northrop T. G., Birmingham T. J., 1982, J. Geophys. Res., 87, 661
Peale S. J., 1976, ARA&A, 14, 215
Peale S. J., 1999, ARA&A, 37, 533
Persoon A. M. et al., 2020, J. Geophys. Res., 125, e27545
Persoon A. M., Gurnett D. A., Kurth W. S., Groene J. B., Faden J. B., 2015, J. Geophys. Res., 120, 6276
Piquette M. et al., 2019, Icarus, 321, 116
Piquette M. R., 2019, PhD thesis, Univ. Colorado Boulder
Poppe A. R. et al., 2019, ApJ, 881, L12
Poppe A. R., 2016, Icarus, 264, 369
Poppe A., James D., Horányi M., 2011, Planet. Space Sci., 59, 319
Porco C. C. et al., 2005, Science, 307, 1226
Postberg F., Kempf S., Hillier J. K., Srama R., Green S. F., McBride N., Grün E., 2008, Icarus, 193, 438
Rein H., Spiegel D. S., 2015, MNRAS, 446, 1424
Renner S., Sicardy B., 2006, Celest. Mech. Dyn. Astron., 94, 237
Roatsch T., Jaumann R., Stephan K., Thomas P. C., 2009, Cartographic Mapping of the Icy Satellites Using ISS and VIMS Data. Springer Science+Business Media, Berlin, Germany, p. 763
Roberts J. H., Stickle A. M., 2017, in Lunar and Planetary Science Conference. Lunar and Planetary Science Conference, The Woodlands, Texas, USA, p. 1955
Robutel P., Laskar J., 2001, Icarus, 152, 4
Sfair R., Giuliatti Winter S. M., 2012, A&A, 543, A17
Showalter M. R., de Pater I., Lissauer J. J., French R. S., 2019, Nature, 566, 350
Šidlichovský M., Nesvorný D., 1996, Celest. Mech. Dyn. Astron, 65, 137
Sinclair A. T., 1972, MNRAS, 160, 169
Sittler E. C. J., Johnson R. E., 2015, in AGU Fall Meeting Abstracts. p. P43E–08
Spahn F. et al., 2006, Planet. Space Sci., 54, 1024
Spahn F., Sachse M., Seiß M., Hsu H.-W., Kempf S., Horányi M., 2019, Space Sci. Rev., 215, 11
Spitale J. N., Jacobson R. A., Porco C. C., Owen W. M. Jr, 2006, AJ, 132, 692
Srama R. et al., 2020, in European Planetary Science Congress. p. EPSC2020
Stooke P. J., 1994, Earth Moon Planets, 65, 31
Sun K.-L., Schmidt J., Spahn F., 2015, preprint (arXiv:1510.07730)
Sun K.-L., Seiß M., Hedman M. M., Spahn F., 2017, Icarus, 284, 206
Synnott S. P., 1986, Icarus, 67, 189
Thomas P. C., Burns J. A., Hedman M., Helfenstein P., Morrison S., Tiscareno M. S., Veverka J., 2013, Icarus, 226, 999
Tseng W. L., Ip W. H., Johnson R. E., Cassidy T. A., Elrod M. K., 2010, Icarus, 206, 382
Tseng W.-L., Ip W.-H., 2011, Icarus, 212, 294
Ye S. Y., Gurnett D. A., Kurth W. S., Averkamp T. F., Morooka M., Sakai S., Wahlund J. E., 2014a, J. Geophys. Res., 119, 3373
Ye S. Y., Gurnett D. A., Kurth W. S., Averkamp T. F., Kempf S., Hsu H. W., Srama R., Grün E., 2014b, J. Geophys. Res., 119, 6294

This paper has been typeset from a TEX/LATEX file prepared by the author.

Downloaded from https://academic.oup.com/mnras/article/511/3/4202/6462913 by INIST-CNRS INSU user on 20 April 2023